

Design & Optimization of Linear Doubly-Fed Induction Machine for Wireless Charging Operation of Novel Vactrain System

Thesis Report

Belkassem Becetti



Design & Optimization of Linear Doubly-Fed Induction Machine for Wireless Charging Operation of Novel Vactrain System

Thesis Report

by

Belkassem Becetti

to obtain the degree of Master of Science
at the Delft University of Technology,
to be defended publicly on Thursday July 29, 2021 at 13:00.

Student number: 4994132
Project duration: November 9, 2020 – July 29, 2021
Thesis committee: Prof. dr. ir. P. Bauer, TU Delft, Supervisor
Dr. J. Dong, TU Delft, Daily Supervisor
Dr. D. J. P. Lahaye, TU Delft, External Member

An electronic version of this thesis is available at <http://repository.tudelft.nl/>.

Acknowledgements

I greatly value the experience and knowledge I gained from this thesis project. The time I spent in Delft will forever be remembered and cherished. Pursuing a master's degree at TU Delft is the opportunity of a lifetime and I will always be in debt to the Foundation Justus Louise van Effen for offering me their full excellence scholarship which enabled me to turn a dream into reality with minimal financial burden on my family.

Over the past two years, I met truly amazing people that contributed significantly towards my development as a person and as an engineer. First of all, I would like to express my immense gratitude towards my thesis daily supervisor, Dr. Jianning Dong. His guidance and mentorship were instrumental in aiding me towards the completion of this project. He demonstrated unending support and patience during this thesis. He was always available for my questions and doubts. He constantly encouraged me and kept pushing me up until the last minute to get the best out of me. His passion for the subject and determination are inspiring and motivating. It was an absolute honor and pleasure to work under his supervision and to attend his courses as well. I would like to also thank Professor Pavol Bauer and Dr. DJP Lahaye for their valuable input and advice.

I cannot express enough appreciation to my family and friends who have been encouraging and were always there for me when I needed them. The abundant care and support I received from my family and especially from my parents and my sister Dr. Karima Becetti were vital to my progression in the master program. My dearest friends at Delft, Mohammed El-Hayek, Serge Saaybi and Avinash Kalloe who I was extremely lucky to meet on day one and have been together ever since, they made the past months bearable and fun. The Corona gang members, Anand, Bram and Rohan who I could not have made it without them through the most difficult courses of the program during the worst period of the pandemic. Lastly, I would like to thank the staff of the InHolland university of applied sciences for allowing students to access their building during the lockdown and use their facilities without requesting permission.

Abstract

With the aim to reduce the CO₂ emissions in the transportation sector, there have been significant developments in the recent few years where novel ground transport systems operating at airline speeds using all-electric propulsion have emerged to provide a sustainable alternative to classical methods of transport such as air travel. These novel systems however use sub-systems for suspension and propulsion that produce significant power loss when compared to traditional rail on wheels. Hence, the aim of this project is to investigate a new system proposed in [1] which aims to use the same concept of Hyperloop involving pods traveling at high speeds in vacuum tubes to minimise drag and thus reduce the energy requirements as well. Unlike Hyperloop, the system aims to use wheels for suspension and a multi-mode linear motor for charging and propulsion where the power supply is integrated into the overall system.

First, an overview of the system is presented before proceeding to the main content of this thesis where the Linear Doubly Fed Induction Machine (LDFIM), the machine intended to perform the charging operation for the vactrain system, is initially designed using an analytical model based on theoretical equations and formulae which is then validated using the Finite Element Method (FEM). Afterwards, the machine is optimized using the Genetic Algorithm (GA) method to enhance its performance. The optimized model is also validated in FEM and all of the results and design parameters for this specific machine are delivered in this report. It is deduced that the LDFIM is capable of performing according to the required performance standards and a sufficiently high efficiency is achieved.

After completing the design of the LDFIM, an outlook on the system's propulsion is discussed before conducting a benchmarking study where the investigated system is compared to Hyperloop by applying the two concepts in a scenario setting and assessing their performance in a variety of criteria. The results demonstrate the capability of the investigated system in reducing the energy and material requirements for ultra-high speed travel making it a promising candidate for a future transport system.

Contents

Acknowledgements	iii
Abstract	v
1 Introduction	1
1.1 Background	1
1.2 Overview of Investigated Vactrain System	2
1.3 Research Focus & Objectives	4
1.3.1 Research Focus	4
1.3.2 Research Objectives	5
1.4 Thesis Outline	5
2 Vactrain System Design	7
2.1 Vactrain Mission Profile	7
2.2 Vactrain Performance Standards & Requirements	7
2.2.1 Charging	7
2.2.2 Propulsion	9
2.3 Vactrain Electrical Machines	9
2.3.1 Charging	9
2.3.2 Acceleration/Deceleration	9
2.3.3 Coasting	10
3 LDFIM Theory & Analytical Design	11
3.1 LDFIM Theory & Principle of Operation	11
3.1.1 LDFIM Background Theory	11
3.1.2 LDFIM Principle of Operation	12
3.2 LDFIM Analytical Design	14
3.2.1 LDFIM Mode of Operation	14
3.2.2 LDFIM Frequency of Operation	15
3.2.3 LDFIM Starting Values & Dimensions	15
3.2.4 LDFIM Pod Coil Design	15
3.2.5 LDFIM Shore Coil Design	17
3.2.6 LDFIM Magnetic Circuit Analysis	20
3.2.7 LDFIM Core Losses	21
3.2.8 LDFIM Equivalent Circuit	22
3.2.9 LDFIM Load Resistance	22
3.2.10 LDFIM Winding Resistances	23
3.2.11 LDFIM Magnetizing Reactance	23
3.2.12 LDFIM Primary Leakage Reactance	23
3.2.13 LDFIM Secondary Leakage Reactance	24
3.2.14 LDFIM Winding Losses	24
3.2.15 LDFIM Performance Calculations	25
3.2.16 LDFIM Forward Model	26
4 LDFIM Finite Element Modeling	29
4.1 LDFIM FEM Model Development	29
4.1.1 Geometry Description	29
4.1.2 Mesh Generation	29
4.1.3 Material & Physics Definition	30
4.1.4 Solving the FEM Model	31

4.2	LDFIM FEM Simulations	31
4.2.1	LDFIM No-Load Test.	32
4.2.2	LDFIM Rated Power Test	33
5	LDFIM Multi-Objective Optimization	37
5.1	Background.	37
5.2	Development of GA Algorithm for LDFIM Optimization	37
5.3	Pareto Solutions & LDFIM Optimized Design	39
5.4	FEM Validation of LDFIM Optimized Design	42
5.4.1	Optimized LDFIM Geometry.	43
5.4.2	Optimized LDFIM No-Load Test	43
5.4.3	Optimized LDFIM Rated Power Test	43
6	Investigated System Benchmarking Against Hyperloop	47
6.1	Investigated System Propulsion	47
6.1.1	LSM for Vactrain Acceleration/Deceleration	47
6.1.2	Vactrain Cruising Subsystem.	48
6.2	Background on Hyperloop	49
6.2.1	System Overview.	49
6.2.2	System Specifications	50
6.3	Suggested Application Scenario	50
6.3.1	Selected Journey	50
6.3.2	Investigated System Storage Specifications	52
6.3.3	Assumptions	52
6.4	Results	53
6.4.1	Journey 1: Dammam to Riyadh	53
6.4.2	Journey 2: Riyadh to Jeddah	54
6.4.3	Complete Journey: Dammam to Jeddah	54
6.4.4	Investigated System Journey Profiles	55
6.4.5	Performance Comparison	55
6.5	Benchmarking	56
7	Conclusions & Recommendations	57
7.1	Conclusions.	57
7.2	Recommendations & Suggestions for Future Work	58

Introduction

1.1. Background

With the threat of climate change being ever-present, a technological revolution is currently underway involving mainly the energy and transportation sectors. The energy transition aims at providing alternatives to conventional energy resources to meet global demands and allow for sustainable development for generations to come by putting a curb on CO₂ emissions and alleviating the effects of climate change. With this energy transition, there is also shift in the transport segment where there is a strong transition towards electric mobility in all modes of travel. Transportation accounts for almost 28% of the global energy consumption according to the most recent edition of the railway handbook by the international energy agency (IEA) as shown in figure 1.1. As well as that, it is considered to be a polluting sector in most industrialized countries due its share of greenhouse gas emissions as shown in figure 1.2 which accounts for nearly a quarter of the global emissions[2]. Decarbonizing the different modes of transport would effectively eliminate a significant portion of the global CO₂ emissions. Therefore, there is a demand and pressure by the world community towards electrifying the transportation industry and providing sustainable alternatives to traditional mobility technologies such as fuel vehicles and airplanes[3].

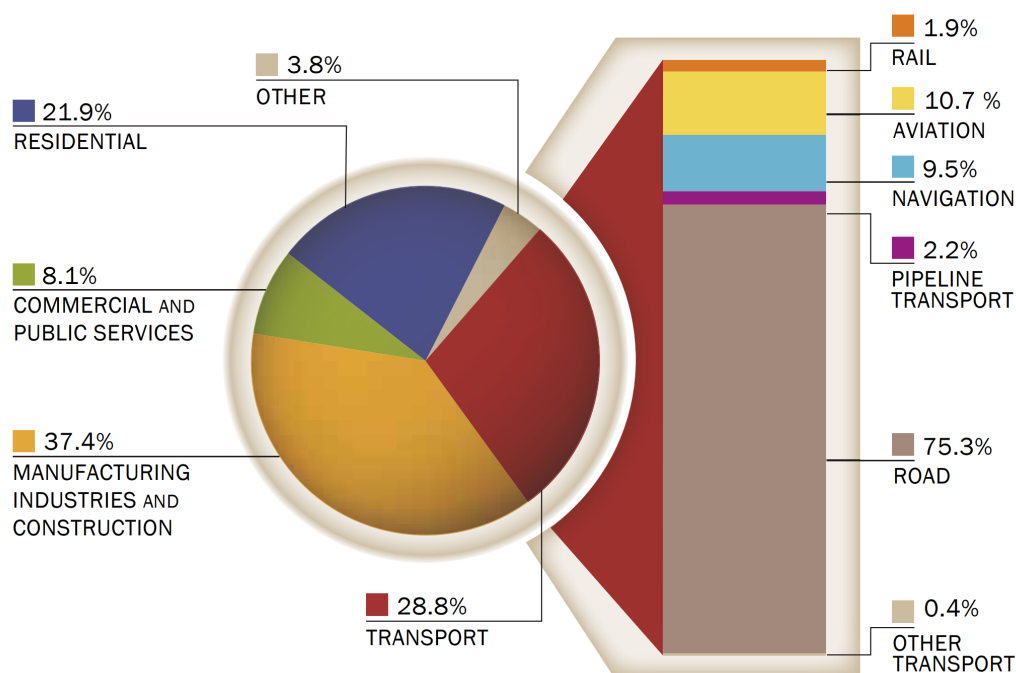


Figure 1.1: Share of Global Energy Demand by Sector from IEA [2]

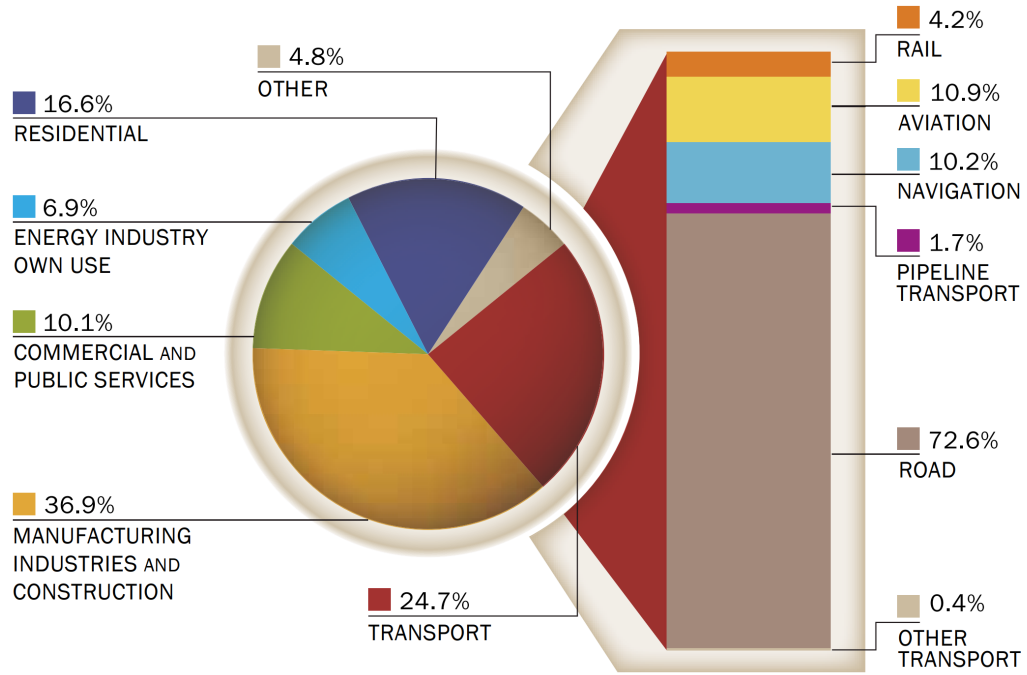


Figure 1.2: Share of Global CO₂ Emissions by Sector from IEA [2]

Consequently, climate change has presented a golden opportunities for the developers of high-speed and ultra high-speed ground transportation systems alike in providing a more economical and environmentally friendly alternative to airplanes for long distance travel. Hence, there are several developments in the ground transportation field including trains at high-speed (TGV) and more recently Hyperloop and Maglev for ultra high-speed systems. These innovative technologies are quite promising in terms of cost and performance since they can operate at significantly high speeds while consuming far less energy than airplanes in linking major cities worldwide and allowing for mass transportation of people and goods. With that being said, there is a novel ultra high-speed ground transportation system being proposed in [1] which suggests the use of wheels on a train track for a vehicle driven in an evacuated tube at extremely low pressure. Using linear motors for charging and propulsion, initial studies of this system demonstrate promising results in terms of efficiency and energy requirements. This has motivated further research into this system for the purpose of carrying out a detailed design and optimization of the necessary linear machines and other components to operate the system according to the specified performance requirements.

1.2. Overview of Investigated Vactrain System

The ultra high-speed vactrain system proposed in [1] consists mainly of a vehicle in the form of a pod carrying passengers being driven on rail tracks using wheels inside an evacuated tube where the air pressure is maintained at an extremely low value of 300 Pa to reduce the aerodynamic drag experienced by the vehicle when in motion. Indeed, the coefficient of rolling resistance for wheel-driven vehicles is low and constant for all speeds. As well as that, using wheels would result in fewer losses and initial cost of implementation. The effect of using wheels inside an evacuated tube is shown in figure 1.3. The figure shows a log-log plot for the drag coefficient against the cruising speed. The drag coefficient is a unitless quantity used to estimate the force experienced by a moving object according to the following formula[4]:

$$F_{drag} = mgC_d \quad (1.1)$$

The coefficient C_d varies depending on the speed and cruising mechanism and the quadratic relationship between drag and speed is clearly observed. Novel ultra-high speed vactrain systems such as Hyperloop suggest mainly the use of electro-dynamic suspension (EDS) or electro-magnetic suspension (EMS) to suspend the vehicle. These systems are considered to be lossy as they result in a much higher drag coefficient for the same speed of operation. With regards to EDS, the drag becomes almost similar to that of an airplane

or a commercial train only at a speed range higher than 200 m/s. In the case of EMS, active high bandwidth control and a high cost track are required. Hence, the authors in [1] make a sound argument with the use of wheels to suspend the vehicle inside evacuated tubes instead of using EDS or EMS. Effectively, the data clearly demonstrates that the investigated system will require minimal energy to operate at the same performance standards of other transport systems making it a promising candidate for ultra high-speed rail travel.

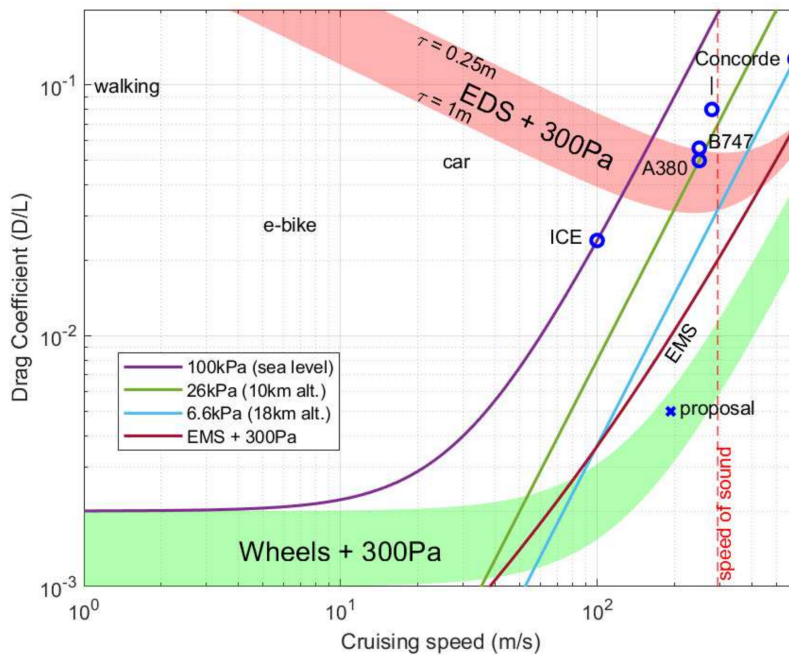


Figure 1.3: Relative drag versus speed[1]

The pod consists of an on-board battery, power electronic converter units and an active coil underneath extending along the length of the pod like a fin. This coil on the pod side will interact with track pads extending along the rail on the shore side to form a linear machine. Different linear machines can be built depending on the component forming the shore side be it an active coil or a passive structure. Since the system is intended to operate at relatively low energy requirements, the mass of the on-board battery will be low depending on the selected battery technology which allows for lightweighting and achieving optimum efficiency[5]. The complete structure of the proposed system is shown in figure 1.4.

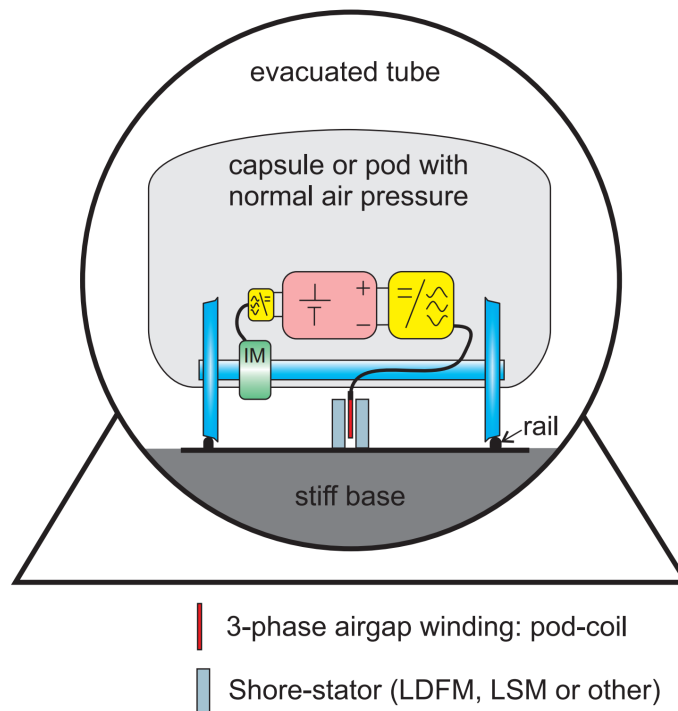


Figure 1.4: Sketch of the pod vehicle to be used in the proposed system[1]

The pod vehicle in the investigated system is intended to operate at the following performance specifications:

- Cruising speed: 700 km/hr
- Passenger capacity: 28 passengers/pod
- Rated Power: 1 MW

The above mentioned performance expectations give this suggested system a significant competitive advantage over other ultra high-speed ground transport systems, especially in the low power requirements where the rated specific power of the proposed pod is expected to be 100 W/kg. Moreover, this system presents itself as a viable alternative to air travel since it can reach similar cruising speeds to modern Airbus aircraft using all-electric propulsion and achieving a much higher flow of passengers as demonstrated in [1]. Hence, this system should be used in long distance travel where it can prove its potential and make a difference.

1.3. Research Focus & Objectives

1.3.1. Research Focus

The vactrain system proposed in [1] is briefly outlined to demonstrate its potential in rivaling other ultra high-speed rail concepts in terms of energy efficiency and low cost based on the argument of using a wheel drive in evacuated tubes. The authors present the system from a conceptual point of view where the design and operation are based on simplified assumptions and calculations. The initial results which demonstrate the capability of this system have motivated further research in order to conduct a thorough analysis and perform a detailed design of the linear machines required to operate the train. This thesis project looks into the design, optimization and analysis of the linear doubly-fed induction machine (LDFIM) which is suggested as a candidate to operate the vactrain system. This specific machine will be the main focus of this project but it will not be the exclusive focal point. The design of the machine must also take into account the overall system since a specific component of the vactrain which is the pod coil will be the backbone of the comprehensive design procedure as it is intended to perform a vital role in every step of the train operation.

1.3.2. Research Objectives

The main objective of this thesis project is to perform a detailed design, analysis and optimization of the LDFIM to operate the proposed vactrain system according to the same performance requirements as outlined in [1] accompanied by an overall system design to build the necessary framework that would enable and motivate further research into this novel ultra high-speed rail system. The aim of this work is to complete a significant step in the complete development of the vactrain system of interest and present a reference for future studies and research into the design of the other required components to complement the machine which will be discussed thoroughly in this project. To achieve this principal objective, the following sub-objectives need to be defined and achieved:

- Develop the most optimum mission profile to operate the vactrain system according to the standards in [1]
- Select the most suitable electrical machine to operate the vactrain system for each phase of the mission profile
- Theoretically design the LDFIM using analytical equations, magnetic circuit analysis and per-phase equivalent circuit performance calculations
- Validate theoretical design of the LDFIM by analyzing its electromagnetic behavior by simulating its performance and operation using Finite Element Modeling (FEM)
- Optimize the design parameters of the LDFIM using Multi-Objective Optimization
- Develop an argument-driven comparative analysis between the investigated system and Hyperloop.

It is important to note that the scope of this thesis project is bound to the analysis, design and optimization of the LDFIM with a particular focus on the overall system design. The complete design of the other system components is not included where certain assumptions will be made to facilitate the research work carried-out in this project.

1.4. Thesis Outline

In order to achieve the aforementioned objectives, the report of this thesis project is outlined as follows:

- Chapter 2: This chapter discusses the mission profile and operation of the train according to the requirements and standards in [1]
- Chapter 3: The aim of this chapter is to present the theory and principle of operation of the LDFIM along with the complete analytical design of the machine
- Chapter 4: The analysis of the electromagnetic behavior of the machine along with the validation of the theoretical design using FEM simulation will be explained in this chapter
- Chapter 5: The focus of this chapter is the optimization of the LDFIM parameters using multi-objective optimization
- Chapter 6: This chapter presents the comparative analysis of the investigated system and Hyperloop to demonstrate the potential of the former in providing low cost transportation at ultra-high speed.
- Chapter 7: This is the final chapter of the thesis report where conclusions are drawn and recommendations are presented for future research work into this topic

2

Vactrain System Design

2.1. Vactrain Mission Profile

The first step in developing a transport system is defining its mission profile which outlines its set of operating conditions and requirements necessary to accomplish its intended objectives under specific performance constraints[6]. For this proposed system, the mission profile will help in identifying the required machinery and components necessary to operate the vactrain as proposed in [1]. Hence, the following list outlines the suggested mission profile for the vactrain system which constitutes the different phases of its journey from station A to station B:

- Phase 1: The vactrain is parked at station A, its point of departure. The on-board battery is charged to the required amount of energy. This amount depends on the cruising speed and range of the vactrain to complete the journey.
- Phase 2: Once charging is complete, the vactrain accelerates from rest and reaches its intended final velocity prior to cruising.
- Phase 3: When the train reaches its cruising speed, acceleration ends and the coasting phase commences. This is the longest phase of the journey where the vactrain operates at its highest speed.
- Phase 4: As the train approaches station B, the regenerative deceleration phase commences where the vactrain's speed is gradually reduced to zero while its kinetic energy is recovered to recharge the on-board battery. When the vactrain reaches zero speed, it should have arrived at station B and the cycle restarts for the next journey.

2.2. Vactrain Performance Standards & Requirements

With the vactrain mission profile defined, the next step would be to look into the operation of the train from a system point of view according to the performance requirements listed in chapter 1. This is done by analyzing the top-level functions required to achieve the overall system objectives. It is important to note that the analysis performed at this stage of the report will involve calculations using expressions and functions relating the different parameters rather than using exact figures. This is because the objective is to observe how the variables of the top-level functions are coupled to the operating specifications of the vactrain which would provide a basis for the detailed design of the required machinery and components later on. The main functionalities of this novel ultra high-speed train system are charging and propulsion.

2.2.1. Charging

This project suggests the utilization of dynamic wireless charging to store energy in the pod's on-board battery which will act as the train's power supply via the power electronic interface. Since this is an ultra high-speed vactrain, it would not be possible to use the traditional pantograph-based system due to friction and arcing. Consequently, it is important to analyze the charging operation of the vactrain as it is responsible for the definition of key system parameters such as battery mass and charging time. These parameters depend mainly on certain operating conditions such as charging power, cruising speed, range and the type of technology

used for the on-board battery. The purpose of the charging function is to store the kinetic energy required to launch the train as well as the amount of energy that would be lost due to drag when cruising. These two energy requirements will be evaluated independently since they represent two different design aspects. The first aspect regarding the required kinetic energy for launching the train will determine the cruising speed the train will reach after accelerating as:

$$\begin{aligned}\frac{1}{2}m_{pod}v_m^2 &= W_{Sbat}m_{bat} \\ v_m &= \sqrt{2W_{Sbat}\frac{m_{bat}}{m_{pod}}}\end{aligned}$$

Where m_{pod} is the mass of the pod and total payload in kg, v_m is the pod speed in m/s, W_{Sbat} is the specific energy of the battery technology in J/kg and m_{bat} is the mass of the on-board battery in kg. Also, it is useful to express the reachable cruising speed as a function of the ratio k_{bat} which indicates the mass of the battery m_{bat} as a fraction of the total pod weight m_{pod} as shown in [1]. As a result, the following equation is obtained:

$$v_m = \sqrt{2W_{Sbat}k_{bat}} \quad (2.1)$$

Therefore, equation 2.1 shows the influence of the parameter k_{bat} on the attainable speed of the vactrain after launch which is a crucial design parameter for the overall system design. Another parameter related to the charging function is the achievable range of the vactrain required to complete its intended journey. The range of the system is evaluated by considering the work done by the train in overcoming drag losses when cruising as follows:

$$\begin{aligned}m_{bat}W_{Sbat} &= C_{drag}m_{pod}g\Delta x \\ \Delta x &= \frac{W_{Sbat}}{C_{drag}g}\frac{m_{bat}}{m_{pod}}\end{aligned}$$

Where C_{drag} is the coefficient of rolling resistance for wheels which when multiplied by the mass of the pod and the acceleration due to gravity g gives the drag force due to suspension on wheels as shown previously in equation 1.1 and Δx is the achievable range or displacement in meters. As with the cruising speed, the attainable range of the vactrain can be expressed using the parameter k_{bat} as:

$$\Delta x = k_{bat}\frac{W_{Sbat}}{C_{drag}g} \quad (2.2)$$

Another important design parameter related to the charging function is the charging time. After determining the cruising speed and the required range to complete the journey, the energy requirements for the vactrain are then well-defined. The remaining parameter is the charging time which depends mainly on the power by which the pod is charged and some of the aforementioned quantities as follows:

$$\begin{aligned}m_{bat}W_{Sbat} &= P_{pod}T \\ T &= \frac{W_{Sbat}m_{pod}}{P_{pod}}\end{aligned}$$

Where P_{pod} is the rated charging power of the pod in W, assuming constant power charging, which is used to determine charging time T based on the amount of energy to be stored in the on-board battery. The charging time can also be expressed in a more useful manner by introducing another term relating the rated power of the pod P_{pod} and its total mass m_{pod} . This term is known as the specific power of the vactrain system p_{spec} measured in W/kg which enables a general approach to the overall system design and making it comparable to other transport systems[1]. Consequently, the charging time is now expressed as:

$$T = W_{Sbat}\frac{k_{bat}}{p_{spec}} \quad (2.3)$$

Equations 2.1, 2.2, 2.3 demonstrate how the parameter k_{bat} is crucial to the overall charging operation and so it needs to be carefully calculated when sizing the overall vactrain system. The specific power of the pod p_{spec} is an important operational parameter which is selected based on the performance requirements of the vactrain.

2.2.2. Propulsion

In this project, the term propulsion deals with the acceleration, deceleration and cruising operations of the vactrain. The cruising operation mainly affects the charging function of the system as discussed in the previous section and so it will not be emphasised in this section. When analyzing the vactrain's propulsion, the main focus will be on the acceleration and deceleration operations. It suffices to study the acceleration of the vactrain since its deceleration is almost the exact opposite from an operational point of view. The purpose of the propulsion function is to provide the means to move or propel the pod by converting the energy stored in the on-board battery into useful mechanical power to increase or maintain the system's kinetic energy.

To analyze the acceleration operation of the vactrain, the most important aspect to inspect is the launching mode of the pod. According to Newton's laws of motion, there are two main launch modes for any transportation system, namely constant acceleration and constant power[7]. According to the authors in [1], it is advantageous to apply constant power launch due to the following reasons:

- There are certain limitations on the electric current in the pod coil, the power electronic converter and the on-board battery in order to limit the heating of these components. By definition, a current limit implies a power limit.
- Controlling the battery discharge rate to be constant at all times during the acceleration phase will result in the least amount of stress applied to it.
- Using constant power launch will reduce the required distance to reach the target speed for the same power by one-third.

Therefore, the constant power mode is selected to operate the vactrain system and this will play a vital role in the selection of the suitable electric machinery to achieve the required functionalities.

2.3. Vactrain Electrical Machines

After defining the vactrain's mission profile and its performance requirements, the next step in the overall system design is selecting the required electric machines required to operate the train. As suggested in [1], the proposed system will use a polymodal linear machine on wheels to perform the necessary functionalities. This linear machine is developed by the electromagnetic interaction between the pod side coil and the various track-type structures. Different types of linear machines can be formed such as a doubly-fed induction machine, synchronous machine, induction machine and synchronous reluctance machine. For each operation of the train in the mission profile, the most suitable machine will be selected according to the performance requirements.

2.3.1. Charging

The only topology capable of fast-charging the on-board battery is the doubly-fed induction machine which has two active sides where the shore track at the station has coils connected to the grid via converters that can transfer the rated power to the pod side wirelessly. This machine is the main focus of this thesis project as it will be designed and optimized. As well as that, the machine will be compared to another commonly used technology for wireless charging to validate the choice for this specific operation.

2.3.2. Acceleration/Deceleration

A significant amount of thrust is required to launch the vactrain using constant power at rated conditions. This limits the choice of topology for this operation to two options which are the linear doubly-fed induction machine and the linear synchronous machine. The problem with using the former is much higher cost of implementation where an active shore track of several kilometers fed by AC supply is required to accelerate the train using high power. Unless this power is supplied from an independent source, it will severely impact the grid. Whereas with the linear synchronous machine, the shore track will consist of permanent magnets or active excitation coils fed by DC supply which would reduce the cost and external power supply requirements considerably and would still enable the pod to generate a relatively high amount of thrust for propulsion from the on-board battery via the pod coil. Therefore, the selected machine to accelerate the vactrain is the linear synchronous machine which is also selected to perform regenerative deceleration since it is able to efficiently recover the train's kinetic energy and recharge the on-board batteries[8].

2.3.3. Coasting

This represents the longest phase of the system's mission profile in terms of both time and distance. Therefore, the selected topology must be low-cost and efficient. It was concluded in a previous study [9] that the linear induction machine is not a suitable candidate for this operation as it would operate on a poor power factor. Also, the linear synchronous reluctance machine as explained in [1] operates at low efficiency and poor power factor. Therefore, it is preferred to equip the pod with a relatively small rotating machine that can be used exclusively for this operation but also can perform as a back-up in case of failure. The authors in [1] suggest using a rotating induction machine but there is also the possibility of using a rotating permanent magnet assisted synchronous reluctance machine which is making significant advances in the automotive industry due to its higher efficiency and power density[10].

3

LDFIM Theory & Analytical Design

3.1. LDFIM Theory & Principle of Operation

3.1.1. LDFIM Background Theory

The LDFIM is the linear counterpart of the conventional rotational doubly fed induction machine. The latter is mainly used as a generator to produce electricity in wind turbines as it is able to perform over a wide speed range and maintain constant synchronization with the electrical grid. The doubly fed induction generator (DFIG) is an induction machine topology where the stator is directly connected to the grid and the rotor is formed by windings and is connected to the grid via a power electronic converter. Both the stator and the rotor of the DFIG are connected to electrical sources which explains the use of the doubly-fed term where electrical power can flow either through the rotor or the stator depending the operating conditions of the machine[11]. The diagram in figure 3.1 shows how the DFIG is used to convert wind energy into electricity for the grid.

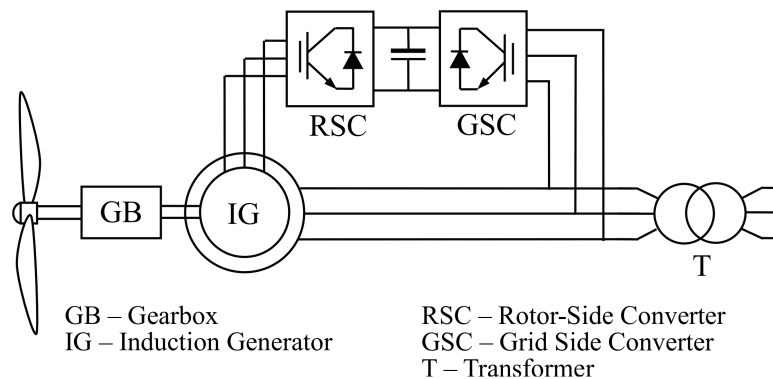


Figure 3.1: Typical Connection of DFIG to the Electrical Grid[11]

The LDFIM is obtained by cutting the rotating counterpart and unrolling it flat. This imaginary process as shown in figure 3.2 can be applied to virtually any rotational electrical machine in order to build its linear version. Almost every electrical machine exists in both rotational and linear modes. Linear machines have existed for more than a century and have now found prospects for various applications in modern transportation systems. Unlike the rotational electrical machine, the linear version does not require the use of gears or mechanical motion converters. However, the main issues arising from the use of linear machines is the fact that they exhibit larger air gap lengths and the presence of edge effects due to the finite length of the primary and secondary components. This inevitably results in low efficiencies and poor power factors. Therefore, the conventional design criteria used to evaluate the performance of rotational machines are not applicable in the case of linear machines[12].

Similarly to the DFIG, the LDFIM has two main components being the primary and the secondary which are equivalent to the stator and rotor in the rotational setting. The primary of the LDFIM is composed of

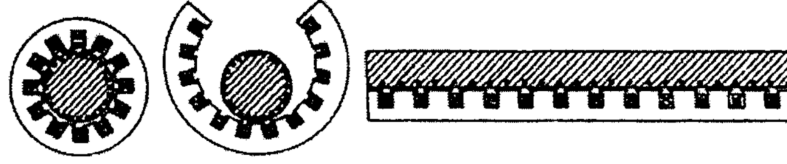


Figure 3.2: The Imaginary Process of Unrolling a Rotating Machine to Obtain the Linear Counterpart[12]

polyphase windings inserted into a slotted iron core while the secondary is formed by coreless windings embedded in an insulating material such as epoxy resin. Eliminating the use of iron in the secondary side of the machine which is part of the pod, allows the vehicle to be lightweight and enables the propulsion of the vac-train to be more efficient as shown in [1]. This then requires the use of a double sided primary where there are two iron cores with windings fixed to the track on both sides of the secondary in order to close the path of the magnetic flux lines in the equivalent magnetic circuit. This specific topology will be used for the fast charging operation of the vac-train where power from the grid connected primary will be transferred to the secondary side pod windings to charge the on-board battery with sufficient energy for the subsequent propulsion and coasting operations. In this report, the primary windings on both sides will be referred to as the shore coil and the secondary windings will be referred to as the pod coil. Figure 3.3 demonstrates the top view of the LDFIM to be designed in this project according to [1].

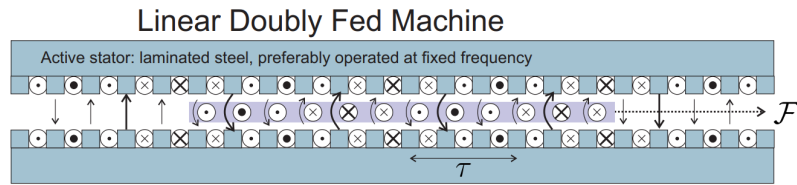


Figure 3.3: Top View of the LDFIM[1]

3.1.2. LDFIM Principle of Operation

The LDFIM is governed by the same operating principle as any induction machine with only minor adjustments to account for its special topology. In this machine, the shore coils being the primary side are excited using a three phase electrical supply to develop a magnetomotive force (MMF) in the air gap and excite the pod coil being the secondary. The latter would then have current induced in it which interacts with the air gap MMF to generate thrust. The main difference between the LDFIM and its rotating counterpart is the fact that the air gap magnetic field generated by the primary windings would not be rotating along the periphery of the machine. Instead, the air gap field will be traveling along the length of the machine in a linear manner and producing a horizontal force from its interaction with the secondary induced currents as opposed to producing rotational torque in the case of the rotating machine. Due to the effect of induction, there will be relative motion between the primary and secondary sides of the machine which is determined by a crucial parameter, the slip s [13]. The slip in rotating induction machines is determined as follows:

$$s = \frac{n_s - n_m}{n_s} \quad (3.1)$$

Where n_s is the synchronous speed of the stator and n_m is the mechanical rotational speed of the rotor in revolutions per minute (rpm). The synchronous speed is defined as follows:

$$n_s = \frac{120f}{p} \quad (3.2)$$

Where f is the stator supply frequency and p is the number of poles of the machine. Equations 3.1 and 3.2 apply specifically for rotating induction machines. For linear machines, the slip is determined as:

$$s = \frac{v_s - v_m}{v_s} \quad (3.3)$$

Where v_s is the synchronous linear speed of the shore side and v_m is the mechanical linear speed of the pod side in meters per second (m/s). The synchronous linear speed is defined as follows:

$$v_s = 2f\tau \quad (3.4)$$

Where τ is the pole pitch of the machine. It is important to note that in the case of linear machines, the synchronous speed of the primary side is influenced by the pole pitch and frequency only and regardless of the number of poles in the machine. The pole pitch τ is the distance from the center of one pole to its neighbour along the circumference of a rotating machine which is equivalent to the longitudinal length of the linear machine as shown in figure 3.4.

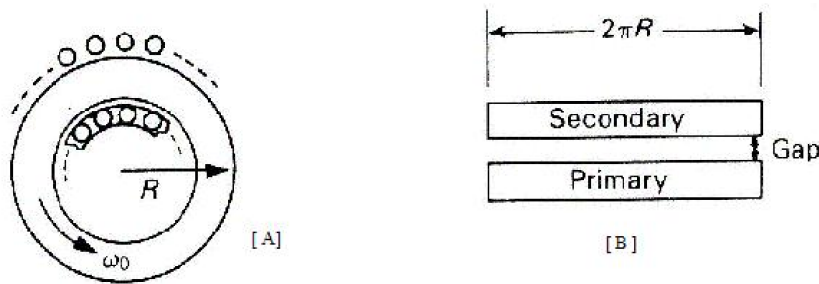


Figure 3.4: Circumference of Rotating Machine & Length of Linear Machine Relation [12]

Therefore, the pole pitch of a linear machine is defined as:

$$\tau = \frac{L}{p} \quad (3.5)$$

Where L is the longitudinal length of the linear machine[13].

Equation 3.3 applies for a linear induction machine (LIM) that is composed of an active primary and a passive secondary. In the case of the LDFIM specific to this project, both shore and pod coils are active since they are connected to electrical sources with specified supply frequencies resulting in two synchronous speeds. This indeed has an effect on the operation of the machine as the mechanical speed of the pod will be defined as follows:

$$v_{pod} = v_m - v_{shore} \quad (3.6)$$

Where v_{pod} is the synchronous speed of the pod coil, v_{shore} is the synchronous speed of the shore coil and v_m is the resultant mechanical speed. By substituting equation 3.6 into equation 3.3 assuming that v_s is v_{shore} , the slip of the LDFIM becomes:

$$s = \frac{-v_{pod}}{v_{shore}} \quad (3.7)$$

Then with the use of equation 3.4, the slip of this machine becomes a fraction of the pod and shore coils' supply frequencies as follows:

$$s = \frac{-f_{pod}}{f_{shore}} \quad (3.8)$$

Effectively, the slip of the LDFIM will be determined by the supply frequencies to the shore and pod coils which are controlled in order to designate the machine's mode of operation[1].

3.2. LDFIM Analytical Design

3.2.1. LDFIM Mode of Operation

The LDFIM can operate in three different modes just as any induction machine which are motoring, generating and plugging. The slip of the machine determines its speed and thereby the mode of operation. The relation between the slip and the speed and thrust of the machine can be interpreted using the torque-speed curve of the conventional rotating induction machine shown in figure 3.5. The curve is applicable for the LDFIM where thrust is plotted on the y-axis instead of torque.

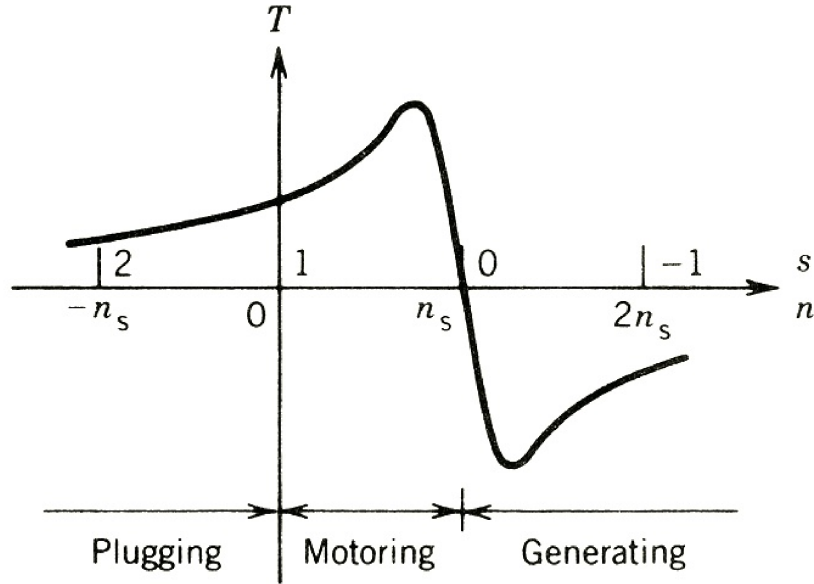


Figure 3.5: Torque-Slip/Speed Curve of Induction Machines[14]

As shown in figure 3.5, the thrust of the LDFIM will vary over a range of speeds according to the slip at which it operates. The important aspect of this feature is the power flow of the machine which would also vary depending on the slip of operation. Thus, the first design step in this project is to analyze the power flow of the LDFIM and determine the most suitable operating conditions for the charging operation of the vactrain. The analysis is performed in the following manner:

$$P_{pod} = P_m - P_{shore} \quad (3.9)$$

As demonstrated in [1], the mechanical power of the pod P_m is the sum of the electrical powers P_{shore} and P_{pod} . Hence, the electrical power of the pod is difference between the shore power and the mechanical power where:

$$P_{pod} = F \times v_{pod} \quad (3.10)$$

$$P_{shore} = F \times v_{shore} \quad (3.11)$$

$$P_m = F \times v_m \quad (3.12)$$

The common element in the above equations is the thrust F measured in Newtons (N) which needs to be developed by the LDFIM to operate the machine. Following on from that, if equations 3.11 and 3.12 are substituted in equation 3.9, the following relation is obtained:

$$P_{pod} = F \left(\frac{v_{shore} - v_m}{v_{shore}} \right) v_{shore} \quad (3.13)$$

Then, with the use of equation 3.3, the slip of the machine is introduced to obtain:

$$P_{pod} = -sFv_{shore} = -sP_{shore} \quad (3.14)$$

Therefore, the power received by the pod coil for charging is the product of the power delivered by the shore coil and the slip. Consequently, maximum power transfer will occur when the slip of the machine $s = 1$. As a result, the pod needs to remain immobile at the station to receive maximum power from the shore side to charge the on-board battery. However, according to equation 3.14, power transfer cannot occur without developing thrust. This then requires the use of a mechanical mechanism to block the pod's movement and keep it in place as demonstrated in [1]. Certainly, the exclusive use of the LDFIM for charging and the requirement of maintaining a constant position of the pod during the operation is beneficial from the design point of view since it allows for more freedom and flexibility in developing the machine to attain the best possible performance parameters.

3.2.2. LDFIM Frequency of Operation

After determining the mode of operation of the machine, the next step is to determine the frequency at which it operates for the charging operation. In order to maximise the charging power of the pod, the slip of the LDFIM needs to be maintained at a value of 1. According to equation 3.8, the slip is the ratio of the pod coil frequency to the shore coil frequency which means that in order to maintain the slip at unity, the pod coil supply frequency needs to be equal to that of the shore coil with an opposite sign that is:

$$f_{pod} = -f_{shore} \quad (3.15)$$

Since both sides of the LDFIM will operate at the same frequency and the machine will be at standstill, this allows for freedom in the choice of frequency of operation. According to [1], the optimal frequency for power transfer would be near the frequency defined by the cross-over speed from constant acceleration mode to constant power mode which is:

$$v_x = \frac{P_{spec}}{a_{max}} \quad (3.16)$$

Where a_{max} is the maximum acceleration of the vactrain during its initial launch. This effectively defines a limit on the operating frequency to be used which is:

$$f_{shore} \leq \frac{v_x}{2\tau} = \frac{P_{spec}}{a_{max}2\tau} \quad (3.17)$$

The authors in [1] use a concept in [15] where a modified formula for core loss is developed which accounts for the differences between static and dynamic hysteresis loops leading to a more accurate method used to extract the loss coefficients of specific core materials. The loss coefficients vary depending on the frequency of operation and therefore, in the case of high frequency machines, the loss coefficients must be accurately estimated as the core loss would play an important role in determining the efficiency of the machine. Based on the concept in [15], the optimal frequency for the LDFIM's charging operation should not be higher than the limit set by equation 3.17 as to avoid excessive core losses. Using the frequency at this limit will be a good balance between reducing losses and increasing the power density of the machine.

3.2.3. LDFIM Starting Values & Dimensions

After determining the mode and frequency of operation for the LDFIM, the design process can be started by first outlining the known design parameters such as the given dimensions and performance requirements according to [1]. The table below shows the known design parameters of the LDFIM:

As well as the known design specifications, other parameters must be assumed in order to commence the design process. The table below outlines the assumed values required to start the design procedure:

As shown in the above table, the peak air gap flux density is assumed to be a relatively low value in order to limit the core losses in the machine and reduce the value of the required magnetizing current as it is expected that the power factor of the machine will be low as compared to rotating machine. Moreover, the assumed value of the current density J is typical for high power linear machines and does not necessitates the use of active cooling systems[13].

3.2.4. LDFIM Pod Coil Design

The design process adopted for this machine is based on the backward method where the intended output power requirements are identified initially by focusing first on designing the pod coil which is the secondary side and then designing the shore coil which is the primary to meet the aforementioned requirements of the secondary side. The first step in the pod coil design stage is the utilization of the fundamental sizing equation

Parameter	Symbol	Value	Unit
Specific Power	p_{spec}	100	W/kg
Frequency	f_{shore}	333.333	Hz
Slip	s	1	N/A
Pod Mass	m_{pod}	10000	kg
Max Thrust	F_{max}	15	kN
Pole Pitch	τ	0.1	m
Number of Poles	p	150	N/A
LDFIM Height	H	0.15	m
LDFIM Length	L	15	m

Table 3.1: List of Known LDFIM Design Parameters

Parameter	Symbol	Value	Unit
Peak Air Gap Flux Density	B_g	0.2	T
Current Density	J	10	A/mm^2
Max Flux Density in Shore Teeth	B_t	1.6	T
Max Flux Density in Shore Yoke	B_y	1.6	T

Table 3.2: List of Assumed LDFIM Design Parameters

which estimates the output coefficient of the machine based on the main dimensions being the length L and height H which form the active area of the LDFIM[16]. According to [1], the developed thrust F is directly proportional to the product of the flux produced by the shore side Ψ_{shore} and the pod coil's amp-turns ni as

$$F \propto \Psi_{shore} \cdot ni \quad (3.18)$$

Where the thrust F is related to the power P via equations 3.10, 3.11 and 3.12.

Equation 3.18 is then used to make a link with the fundamental sizing equation which is

$$\sigma_{Ftan} = \frac{AB_g \cos\zeta}{\sqrt{2}} \quad (3.19)$$

Where A is the linear current density of the pod side measured in A/m which is linked to the pod coil's amp turns ni from equation 3.18, B_g is the peak value of the fundamental air gap flux density which is linked to the shore side flux Ψ_{shore} from equation 3.18 and σ_{Ftan} is the tangential stress or thrust density of the machine measured in N/m^2 which is linked to the thrust F from equation 3.18. The parameter $\cos\zeta$ which is the spatial phase shift between A and B needs to be assumed a suitable operating value at this stage of the design process [16]. Equation 3.19 is then manipulated in order to solve for the required linear current density of the pod coil as

$$A = \frac{p_{spec} m_{pod}}{\sqrt{2} B_g \cos\zeta H \tau^2 p f_{shore}} \quad (3.20)$$

The linear current density A can then be used to determine the expected phase current in the pod coil using the current sheet concept where the coil is modeled to be a smooth surface with infinitely thin current carrying elements with linear current densities measured in A/m as

$$A = \frac{2m N_{pod} I_{pod} k_{wpod}}{p\tau} \quad (3.21)$$

Where m is the number of phases, N_{pod} is the number of series connected turns per phase, I_{pod} is the RMS value of the phase current and k_{wpod} is the fundamental winding factor. The next step is to select the winding configuration of the pod coil in order to determine N_{pod} and calculate k_{wpod} [12].

The pod coil will be used in different stages of the vactrain's mission profile and not only as part of the LDFIM for charging. Therefore, its winding arrangement needs to allow it to be versatile to perform both charging and propulsion. Since this is an air-core coil, it can be designed either using overlapped or non-overlapped windings. The latter is simpler in terms of manufacturing and maintenance but the former results

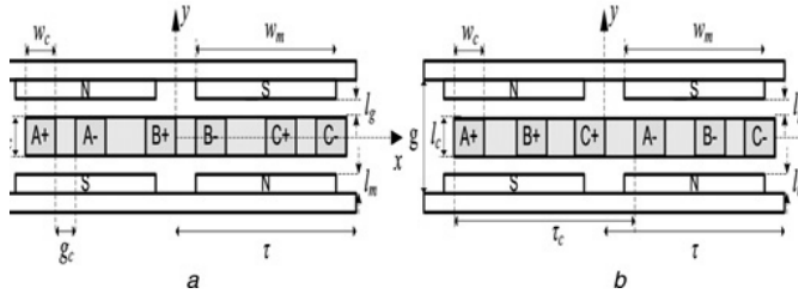


Figure 3.6: Schematic of Permanent Magnet Linear Machine with Air-Core Winding (a. Non-overlapped, b. Overlapped)[17]

in higher values of thrust density and induced voltage[17]. Figure 3.6 demonstrates the difference between overlapped and non-overlapped windings

In order to achieve the best possible performance, the pod coil is to be designed using overlapped windings. Then, the pod coil is analyzed using the winding function theory in order to compute its fundamental winding factor. The number of series connected turns N_{pod} is tentatively selected at this stage of the design process and is validated when the output power requirements of the pod coil are met. Unlike the winding function of slotted windings which is step-wise sinusoidal, the winding function of air-core windings is trapezoidal due to the distribution of windings inside the air core. To calculate the winding factor, the harmonic analysis that was demonstrated in the course ET4121 AC Machines is followed where the turns counting function of the three phase air core winding is determined initially[18]. Figure 3.7 shows the trapezoidal turns counting function for the three phase pod coil along with its winding arrangement

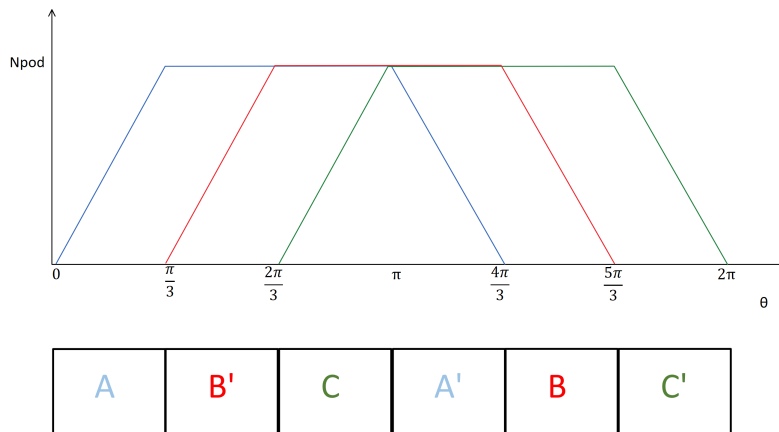


Figure 3.7: Turns Counting Function of Air Core Coil & Winding Arrangement for a Single Pole Pair

With the values of N_{pod} and k_{wpod} being known, the estimated pod coil phase current I_{pod} can be computed using equation 3.21. I_{pod} is then used to estimate the required pod coil conductor area A_{pod} and accordingly the necessary thickness of the pod side t . Since the current density J is already assumed, A_{pod} is calculated as:

$$A_{pod} = \frac{I_{pod}}{J} \tag{3.22}$$

The thickness of the pod coil t is then estimated by accounting for the insulation of the windings and assuming a 50% fill factor. The diameter of the total conductor area with insulation will determine t which is a crucial parameter since it will play an important role in determining the overall length of the air gap which will be discussed at a later stage in this report.

3.2.5. LDFIM Shore Coil Design

The next stage in the backward design of the LDFIM after developing the pod coil winding arrangement and dimensions is the design of the shore coil which is the primary side. The shore coil is responsible for trans-

ferring electrical power to the pod coil and to also magnetize the machine. Therefore, it is necessary to use distributed windings to limit the harmonic content in the MMF of the shore coil. This is a key design choice for the stator of most rotating induction machines[16]. Hence, the winding selected for the shore coil is a distributed double-layer short-pitch winding. Using a two-layer winding arrangement offers the possibility to apply short-pitching allowing for more flexibility in the design of the primary winding. Short-pitching reduces the copper consumption and produces more sinusoidal waveforms where the aim is to mitigate the effects of harmful harmonics such as the fifth and retain a high fundamental factor. A typical double-layer winding arrangement commonly used in linear machines is shown in figure 3.8.

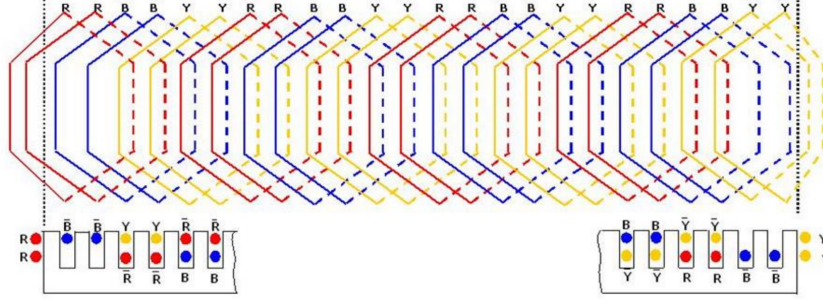


Figure 3.8: Standard Double Layer Winding for Linear Machines[19]

The next step in the design of the shore coil is the selection of the appropriate dimensions and winding arrangement to meet the LDFIM operational and performance requirements. Similarly to the pod coil design discussed previously, the aim of this step is to determine the number series connected turns per phase N_{shore} and the fundamental winding factor k_{wshore} . Since this is a slotted winding structure, N_{pod} is computed as:

$$N_{shore} = \frac{Q \times z_Q}{2am} \quad (3.23)$$

Where z_Q is the number of conductors per slot which needs to be an even integer since the winding is double-layered and a is the number of parallel paths in the winding. Q is the total number of slots on both sides of the LDFIM shore coil and is computed as:

$$Q = 2m \times q \times p \quad (3.24)$$

After setting the number of turns, the fundamental winding factor k_{wshore} is computed analytically as demonstrated in [16] evaluating the product of the pitch factor k_p and the distribution factor k_d as:

$$k_{wshore} = k_p \times k_d \quad (3.25)$$

Where k_p is given by

$$k_p = \sin \frac{\theta_p}{2} \quad (3.26)$$

Where θ_p is the coil span in electrical degrees. The distribution factor k_d is given as

$$k_d = \frac{\sin \frac{\pi}{2m}}{q \sin \frac{\pi}{2mq}} \quad (3.27)$$

With N_{shore} and k_{wshore} determined, the next step is to work out the shore coil dimensions and geometry as shown in figure 3.9 which demonstrates a section of the primary side for a LIM with open slots and the main parameters to be solved[13].

The first parameter to be solved is the slot area which depends on the shore coil current. For the LDFIM, the shore side current I_{shore} is estimated from the ratio of output to input power in the following manner:

$$I_{shore} = \frac{m_{pod} P_{spec}}{3V_{in} \eta \cos \phi} \quad (3.28)$$

Where V_{in} is the RMS value of the input phase voltage which is assumed and η and $\cos \phi$ are the expected values for the efficiency and power factor of the machine respectively. In machine design, the value of the

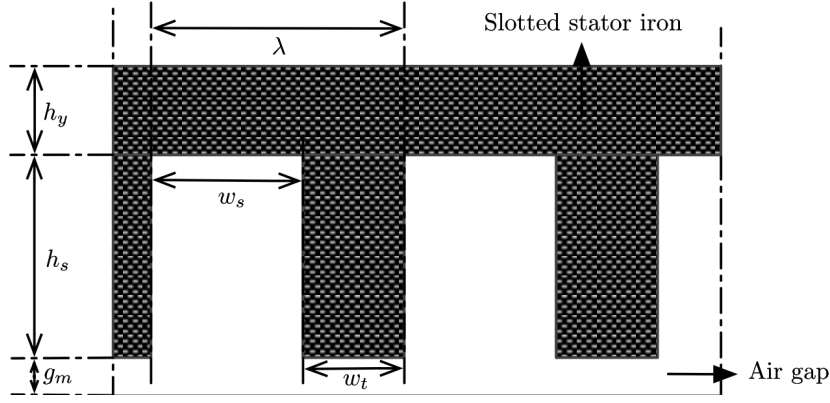


Figure 3.9: Slotted Structure of LIM Primary Side[13]

efficiency and power factor product is assumed at a suitable operating value which is 0.2-0.5 for linear machines[13].

With I_{shore} estimated, the shore side conductor area A_{shore} can be evaluated as:

$$A_{shore} = \frac{I_{shore}}{aJ} \quad (3.29)$$

The area of the slot A_s which encases the conductors is then calculated using the following equation assuming a 50% fill factor due to insulation:

$$A_s = \frac{zQ A_{shore}}{0.5} \quad (3.30)$$

With A_s defined, the remaining geometric parameters can be determined. The slot pitch τ which is defined as the distance between two consecutive teeth on the shore coil is given by:

$$\lambda = \frac{\tau}{mq} \quad (3.31)$$

With λ , the tooth width w_t can be dimensioned in order to limit saturation in the shore teeth and avoid excessive core losses. With the assumed maximum allowable flux density in the teeth B_t , the minimum tooth width w_t is calculated as follows:

$$w_t = \frac{B_g \lambda}{B_t} \quad (3.32)$$

The slot width w_s can then be determined in the following manner:

$$w_s = \lambda - w_t \quad (3.33)$$

The slot height h_s is then given by:

$$h_s = \frac{A_s}{w_s} \quad (3.34)$$

With all slot dimensions defined, the back iron is the next component of the shore coil to be designed. The back iron or yoke is a crucial component of the magnetic circuit as it provides a means to close the flux lines. The height of the back iron h_y needs to be properly sized for the same reasons as the tooth width w_t according to the assumed maximum allowable flux density B_y and is given by:

$$h_y = \frac{\tau B_g}{\pi B_y} \quad (3.35)$$

An important feature to point out is the fact that totally open slots used in linear machines as shown in figure 3.9 result in a significant amount flux leakage and so it is important to limit the slot opening to the air gap while keeping a large enough spacing to allow insertion of conductors into the slots[16]. Therefore, as opposed to using totally open slots, semi-closed slots will be used for the LDFIM with T-shaped teeth to reduce the slot opening.

3.2.6. LDFIM Magnetic Circuit Analysis

After determining the geometry and dimensions of both coils of the LDFIM, it is important to develop the machine's equivalent magnetic circuit and analyze it in order to estimate the required magnetizing current of the machine. The most important aspect of the magnetic circuit for linear machines is the equivalent magnetic air gap length g_e . To calculate this parameter, initially, the total mechanical air gap g_m is defined for the LDFIM which is given as:

$$g_m = t + 2d \quad (3.36)$$

Where t is the thickness of the pod coil in the center of the machine and d is the mechanical clearance separating the pod coil from both sides of the shore coil. Since the LDFIM is to be operated at standstill for charging, it is designated as a low-speed linear machine where the dynamic end effects can be neglected and the mechanical clearance d can be set as low as 1 mm to obtain the smallest possible air gap and reduce the required magnetizing current[8].

Due to the presence of slots in the shore coil, the flux density tends to decrease at the slot opening as shown in figure 3.10 implying that the length of the air gap is longer than the calculated physical dimension[16].

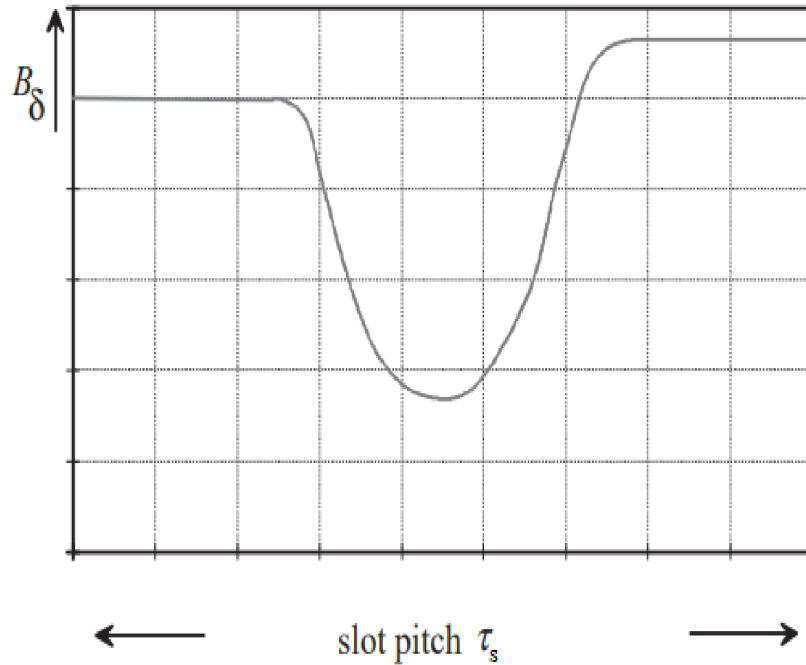


Figure 3.10: The Effect of Slot Opening on the Air Gap Flux Density[16]

To account for the slotting effect, Carter's coefficient k_c needs to be calculated as demonstrated in [8] which is then multiplied by g_m to obtain g_e . k_c is calculated using the following method:

$$k_c = \frac{g_m}{g_e} = \frac{1}{1 - \sigma_c \frac{w_s}{\lambda}} \quad (3.37)$$

Where σ_c is:

$$\sigma_c = \frac{2}{\pi} \arctan\left(\frac{w_s}{2g_m}\right) - \frac{1}{\pi} \frac{2g_m}{w_s} \ln\left(1 + \left(\frac{w_s}{2g_m}\right)^2\right) \quad (3.38)$$

With the equivalent magnetic air gap defined, the analysis of the magnetic circuit can be achieved by computing the different magnetic potentials in the overall magnetic circuit. The main magnetic potential in the LDFIM's equivalent magnetic circuit is due to the air gap flux density. The air gap MMF or magnetic potential F_g is given as:

$$F_g = g_e \frac{B_g}{\mu_0} \quad (3.39)$$

The remaining magnetic potentials are related to the shore's teeth and back iron which are F_t and F_y respectively. These magnetic potentials are determined by the shore coil's core material's BH curve where the value of the magnetic field intensity H corresponding to the maximum allowable flux density B in either the shore teeth or back iron is used to compute teeth and back iron MMFs. The core material selected for the LDFIM is 20WTG1500, a product of the company Baosteel which features high magnetic saturation and is able to reduce the core losses in comparison to other commercially available core materials[20]. The material's BH curve is used to perform the following computations. Since the same value of B is assumed for the maximum allowable flux density in the iron parts of the machine, the same value of the magnetic field intensity H will be used to compute the remaining magnetic potentials.

F_t and F_y are calculated in the following manner[21]:

$$F_t = H \times h_s \quad (3.40)$$

$$F_y = H \times \tau \quad (3.41)$$

The required magnetizing current per phase I_m is then estimated based on the total equivalent MMF of LDFIM F_{eq} which is the sum of the individual MMFs using the following formula[16]:

$$F_{eq} = F_g + F_t + F_y \quad (3.42)$$

$$I_m = \frac{F_{eq} p \pi}{2\sqrt{23} k_{wshore} N_{shore}} \quad (3.43)$$

3.2.7. LDFIM Core Losses

The LDFIM in this project is classified as a high power machine and will exhibit magnetic core losses due to the significant amount of ferromagnetic material used to build the shore coil. Even if the assumed air gap magnetic flux density is relatively small, the core losses will not be negligible and must be accounted for. These losses are estimated by first calculating the total weight of iron used and multiplying it by the specific core loss density from the manufacturer's datasheet. The weight of the iron to be used is calculated in the following manner[13]:

$$V_y = L \times H \times h_y \times 2 \quad (3.44)$$

$$V_t = Q \times H \times w_t \times h_s \quad (3.45)$$

$$W_{iron} = (V_y + V_t) \rho_{iron} \quad (3.46)$$

Where V_y is the volume of the shore back iron on both sides of the LDFIM and V_t is the volume of the machine's teeth. Then the weight of the iron W_{iron} is estimated by multiplying the total volume of the shore's iron by the density of the ferromagnetic material. Hence, the core losses are then estimated by:

$$P_{core} = W_{iron} P_c \quad (3.47)$$

Where P_c is the material's specific core loss measured in W/kg which accounts for both hysteresis loss P_h and eddy current loss P_e as shown in [15]:

$$P_c = P_h + P_e \quad (3.48)$$

$$P_c = k_h \times f \times B^n + k_e \times f^2 \times B^2 \quad (3.49)$$

Where B and f are the flux density and the frequency of the external magnetic field respectively. The coefficients k_h , k_e and n are related to the material's properties. Since the manufacturer's datasheet only provides loss data in tables for specific flux densities and frequencies without presenting the loss coefficients, it is important to extract these coefficients using the method outlined in [15] by generating the loss curves from the datasheet and applying polynomial curve fitting. Table 3.3 outlines the core loss parameters calculated for the core material to be used for the LDFIM

Symbol	Value
k_h	0.0188
k_e	2.79e-5
n	2.364

Table 3.3: Core Loss Parameters

3.2.8. LDFIM Equivalent Circuit

With the dimensions and geometry of the LDFIM defined, the next phase is to develop the machine's equivalent circuit in order to predict its performance and characteristics in a theoretical manner. It is decided for the purposes of this analysis to utilize the IEEE-recommended equivalent circuit shown in figure 3.11 since the air gap of the LDFIM is quite large and the magnetizing current is consequently high also[14]. The subsequent content in this report will demonstrate the methodology employed to compute the different components of the equivalent circuit.

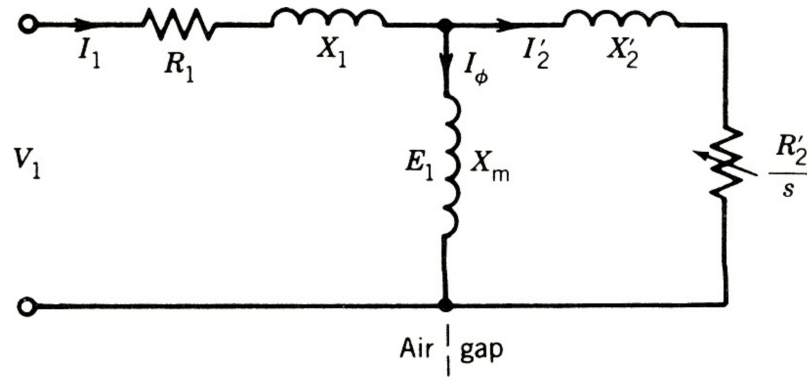


Figure 3.11: IEEE-Recommended IM Equivalent Circuit[14]

It is important to point out that since the LDFIM's slip of operation is set at a value of $s = 1$, the total transferred power from the shore coil will be delivered to the secondary resistance R_2 in the equivalent circuit. This resistance is initially referred to the secondary side and is effectively split into two parts as:

$$R_2 = R_{load} + R_{pod} \quad (3.50)$$

Where R_{load} is the load resistance representing the pod's on-board battery to be charged and R_{pod} is the resistance of the pod coil's windings accounting for the secondary side copper losses.

Equally as important with regards to the equivalent circuit, the shore coil and pod coil represent two different parts of the circuit model since the windings on both sides are configured differently and therefore, the circuit elements in the pod side need to be referred to shore side to form the equivalent circuit in figure 3.11. To achieve this, the turns ratio k_{tr} required to reduce the secondary side to the primary side is defined as follows[13]:

$$k_{tr} = \frac{N_{shore} k_{wshore}}{N_{pod} k_{wpod}} \quad (3.51)$$

This is an important parameter which will play in the analysis of the equivalent circuit after determining the circuit components on a per-phase basis and referring all of them to the primary side.

3.2.9. LDFIM Load Resistance

As mentioned before, R_{load} is the resistance emulated by the on-board power electronic converter to extract the power transferred to the pod coil and charge the pod's battery which is assumed in this case as a purely resistive load. The value of R_{load} can be estimated from the output power requirements of the machine and the expected value of the pod coil phase current I_{pod} calculated using the current sheet concept as per equation 3.21 in the following manner:

$$R_{load} = \frac{m_{pod} P_{spec}}{3(I_{pod})^2} \quad (3.52)$$

This is then designated as the estimated load resistance in the per-phase equivalent circuit representing the useful output power used to charge the pod's battery.

3.2.10. LDFIM Winding Resistances

Both shore and pod coils comprise of windings and their effective resistances will be calculated in the same manner. The winding resistance of the shore coil R_{shore} is equivalent to R_1 in the per-phase equivalent circuit and the pod coil's winding resistance has already been explained. The winding resistances R_{shore} and R_{pod} are given by[8]:

$$l_{endshore,pod} = \frac{\theta_{pshore,coil}}{\pi} \tau \frac{\pi}{2} \quad (3.53)$$

$$l_{wshore,pod} = N_{shore,pod} \times 2(H + l_{endshore,pod}) \quad (3.54)$$

$$R_{shore,pod} = \rho_{copper} \frac{l_{wshore,pod}}{A_{shore,pod}} \quad (3.55)$$

Where $l_{endshore,pod}$ is the length of the end connection in a single turn assuming its shape being semi-circular, $l_{wshore,pod}$ is the total winding length including all series connected turns and ρ_{copper} is the resistivity of copper.

3.2.11. LDFIM Magnetizing Reactance

From the dimensions and geometry of the LDFIM, the magnetizing inductance L_m is given by[16]:

$$L_m = \frac{12\mu_0(k_{wshore}N_{shore})^2 H\tau}{g_e \pi p} \quad (3.56)$$

Thus, the magnetizing reactance X_m is calculated as:

$$X_m = 2\pi f_{shore} L_m \quad (3.57)$$

3.2.12. LDFIM Primary Leakage Reactance

In both coils of the LDFIM, there is leakage flux that does not contribute towards linking the primary and secondary sides together as opposed to the main flux which is represented by the magnetizing inductance L_m . Therefore, there leakage inductances on both sides of the machine that result in the aforementioned leakage flux[16]. With regards to leakage inductance of the shore coil, it comprises of the following:

- Slot Leakage Inductance
- Differential Leakage Inductance
- End Connection Leakage Inductance

All three leakage inductances are computed together to obtain the overall primary side leakage inductance L_1 in the following manner[8]:

$$L_1 = \frac{4\mu_0}{pq} [(\lambda_{slot} + \lambda_{diff})H + (\lambda_{end}nd \times (l_{endshore}))](N_{shore})^2 \quad (3.58)$$

Where λ_{slot} is the slot specific permeance calculated as:

$$\lambda_{slot} = \frac{h_s(1 + 3\frac{\theta_p}{\pi})}{12w_s} \quad (3.59)$$

As well as that, λ_{diff} is the differential leakage permeance which in the case of large air gap linear machines such as the LDFIM is rather low, $\lambda_{diff} < 0.2$ and λ_{end} is the coil end connection permeance designated as $\lambda_{end} = 0.33q$ for double-layer windings.

Then, the primary leakage reactance can be determined as follows:

$$X_1 = 2\pi f_{shore} L_1 \quad (3.60)$$

3.2.13. LDFIM Secondary Leakage Reactance

The pod coil's windings are encapsulated in an air-core where no iron or teeth are used. This effectively eliminates slot leakage and allows for the differential leakage to be neglected since it is assumed that there will be negligible harmonic leakage in the pod coil. This means that the only source of flux leakage in the secondary side is due to the end winding connections which is calculated in the same manner as for the primary side. The secondary side leakage inductance L_2

$$L_2 = \frac{4\mu_0}{p} [(0.3(3 \sin \frac{\pi}{2} - 1)(l_{endpod})](N_{pod})^2 \quad (3.61)$$

The secondary side leakage reactance X_2 can then be calculated as:

$$X_2 = 2\pi f_{shore} L_2 \quad (3.62)$$

3.2.14. LDFIM Winding Losses

Since the LDFIM is designed to operate at a relatively higher frequency than most industrial electrical machines, it is important to analyze its most major source of losses which is the ohmic losses in its windings. Due to the effect of eddy currents, a conductor's resistance increases with increasing frequency leading to skin effect. Moreover, when a winding is exposed to an alternating external magnetic field, it will lead to proximity effect. In the LDFIM, both shore and pod coils operate at the same frequency and the pod coil in particular is exposed the main magnetic field induced by the shore coil in the air gap. Therefore, the winding losses for the LDFIM will be analyzed using the method discussed in [22]. Furthermore, it is assumed that Litz wire is used in developing the shore and pod windings in order to limit their losses as compared to the use of traditional round conductors. As well as that, using Litz wire in the pod coil particularly will allow for more freedom and flexibility in the winding arrangement in order to limit its width and reduce the required magnetizing current of the machine.

According to [22], the Litz wire winding losses due to skin effect including DC losses P_{skin} are calculated as:

$$P_{skin} = n \times R_{DC} \times F_R(f) \times \left(\frac{\hat{I}}{n}\right)^2 \quad (3.63)$$

Where n is the number of strands, \hat{I} is the peak current flowing through the conductor and R_{DC} is conductor resistance per meter calculated as

$$R_{DC} = \frac{4}{\sigma \times \pi \times d_i^2} \quad (3.64)$$

Where d_i is the diameter of the individual strand.

Following on from that, the proximity effect losses are computed as a sum of the losses due to the external magnetic field H_e and the losses due to the internal magnetic field H_i . In [22], the proximity effect losses P_{prox} are given as

$$P_{prox} = n \times R_{DC} \times G_R(f) \times \left(\hat{H}_e^2 + \left(\frac{\hat{I}}{2\pi^2 d_a^2}\right)^2\right) \quad (3.65)$$

Where d_a is the diameter of the bundle containing the strands. It is important to note that the factors F_R and G_R depend on the frequency of the current flowing in the conductors and their geometries. They are computed using Kelvin functions as shown in [22].

After computing the skin effect losses P_{skin} and proximity effect losses P_{prox} , they can be summed and multiplied by the length of the series connected turns to obtain the total winding loss P_{loss} for both shore and pod coils. Equations 3.63 and 3.65 can be applied to calculate the shore coil and pod coil winding losses $P_{lossshore}$ and $P_{losspod}$ with the only difference being that the shore coil is not exposed to an external field as is the case for the pod coil. The winding losses are then calculated as:

$$P_{lossshore,pod} = (P_{skinshore,pod} + P_{proxshore,pod}) \times (3 \times N_{shore,pod} \times MLT_{shore,pod}) \quad (3.66)$$

Where MLT is the mean length of a single turn. The winding losses are crucial to the performance of the machine and will be used to assess the efficiency of the LDFIM in the analytical model.

3.2.15. LDFIM Performance Calculations

With the parameters of the per-phase equivalent circuit of the LDFIM defined, the performance of the machine can be estimated using steady-state analysis where the copper losses, power factor and efficiency are calculated. The first step in the steady-state analysis is to obtain the total equivalent impedance Z_{eq} of the LDFIM. To calculate Z_{eq} , the pod coil impedance is referred to the shore coil first, combined in parallel with the magnetizing reactance X_m and then is then added to the shore coil impedance in series[23]. The secondary side impedance Z_2 is calculated as:

$$Z_2 = R_{load} + R_{pod} + jX_2 \quad (3.67)$$

Then the total equivalent impedance Z_{eq} is given as:

$$Z_{eq} = R_1 + jX_1 + \frac{1}{\frac{1}{jX_m} + \frac{1}{Z_2}} \quad (3.68)$$

The phase ϕ of the complex value Z_{eq} represents the angle of the power factor PF where

$$PF = \cos \phi \quad (3.69)$$

The primary side phase current I_1 is then calculated as:

$$I_1 = \frac{V_{in}}{Z} \quad (3.70)$$

With I_1 , the magnetizing current I_m going through the magnetizing branch of X_m and the secondary side current I_2 are computed as follows:

$$I_{mag} = \frac{Z_2}{jX_m + Z_2} I_1 \quad (3.71)$$

$$I_2 = \frac{jX_m}{jX_m + Z_2} I_1 \quad (3.72)$$

The input active power P_{in} can then be given as:

$$P_{in} = 3V_{in}I_1 \cos \phi \quad (3.73)$$

The output power P_{out} is then obtained by subtracting the winding losses on both sides along with the core losses from the input power P_{in} in the following manner:

$$P_{out} = P_{in} - P_{loss,shore} - P_{loss,pod} - P_{core} \quad (3.74)$$

The efficiency η is then calculated as

$$\eta = \frac{P_{out}}{P_{in}} \quad (3.75)$$

Additionally, the peak fundamental air gap flux density B_{ag} can be back calculated from the equivalent circuit by initially computing the resulting MMF Θ_m from I_{mag} as follows:

$$\Theta_m = \frac{2\sqrt{2}I_{mag}3k_{wshore}N_{shore}}{p\pi} \quad (3.76)$$

$$B_{gpeak} = \frac{\mu_0\Theta_m}{g_e} \quad (3.77)$$

This completes the equivalent circuit analysis where the results are compared with the assumed parameters to see if there is a close match. The entire design process is iterated several times until there is a match between the results, the assumptions and the performance requirements of the LDFIM. The purpose of the analytical design of the LDFIM at this stage of the report is to examine the possibility of using this specific machine for charging the vactrain and developing a suitable design for it. Design improvement and optimization will occur at a later stage.

3.2.16. LDFIM Forward Model

Thus far, the design process was based on the backward method where the procedure commenced from the secondary side and progressed backwards towards the primary side. After analyzing the equivalent circuit and finding a suitable design for the LDFIM, a forward theoretical model needs to be implemented where initially, the dimensions, geometry and input phase voltage of the machine are fed as input values and then proceeding to the equivalent circuit analysis as per the previous section to prove the validity and feasibility of the machine. In this section, the parameters of the LDFIM's analytical forward model are tabulated to conclude this chapter of the report.

Parameter	Symbol	Value	Unit
Shore Coil Slots per Pole per Phase	q	2	N/A
Shore Coil Pitch Angle	θ_{pshore}	$\frac{5}{6}\pi$	rad
Shore Coil Parallel Paths	a	2	N/A
Shore Coil Series Connected Turns per Phase	N_{shore}	300	N/A
Shore Coil Fundamental Winding Factor	k_{wshore}	0.933	N/A
Shore Coil Conductor Area	A_{shore}	3.85e-5	m^2
Shore Coil Slot Area	A_s	1.54e-4	m^2
Shore Coil Slot Pitch	λ	0.0167	m
Shore Coil Slot Opening	w_s	0.0105	m
Shore Coil Slot Height	h_s	0.0129	m
Shore Coil Tooth width	w_t	0.0048	m
Shore Coil Back Iron Height	h_y	0.0068	m

Table 3.4: LDFIM Shore Coil Parameters

Parameter	Symbol	Value	Unit
Pod Coil Pitch Angle	θ_{ppod}	π	rad
Pod Coil Series Connected Turns per Phase	N_{pod}	150	N/A
Pod Coil Fundamental Winding Factor	k_{wpod}	0.9549	N/A
Pod Coil Conductor Area	A_{pod}	9.25e-5	m^2
Pod Coil Thickness	t	0.0115	m
Mechanical Clearance	d	1	mm
Magnetic Air Gap Length	g_e	0.0146	m

Table 3.5: LDFIM Pod Coil Parameters

Parameter	Symbol	Value	Unit
Input Phase Voltage (RMS)	V_{in}	1130	V
Shore Coil Resistance	R_1	0.0368	Ω
Pod Coil Resistance	R_{pod}	0.0639	Ω
Load Resistance	R_{load}	1.5084	Ω
Shore Coil Leakage Reactance	X_1	0.4941	Ω
Pod Coil Leakage Reactance	X_2	0.5683	Ω
Magnetizing Reactance	X_m	1.7157	Ω
Turns ratio	k_{tr}	1.9542	N/A

Table 3.6: LDFIM per Phase Equivalent Circuit Parameters Referred to the Shore/Primary Side

Parameter	Symbol	Value	Unit
Parameter	Symbol	Value	Unit
Air Gap Flux Density	B_{ag}	0.2	T
Power Factor	PF	0.431	N/A
Input Power	P_{in}	1.12	MW
Output Power	P_{out}	1	MW
Efficiency	η	89.45%	N/A

Table 3.7: LDFIM Theoretical Performance Measures

4

LDFIM Finite Element Modeling

4.1. LDFIM FEM Model Development

The finite element method (FEM) is a powerful engineering tool very often used in the design of electrical machines. Experience in machine design has shown that theoretical models cannot be depended on solely and therefore, modern simulation tools involving FEM are extensively used to validate theoretically developed designs by analyzing their electromagnetic behaviour[13]. The FEM model developed for the LDFIM in this project is accomplished using the software COMSOL. This is realized by initially defining a magnetic fields problem and setting it in a two-dimensional domain where the machine parameters can be defined and simulated. The purpose of the FEM simulation is to solve the problem and find a solution for the magnetic vector potential A_m in the model of the LDFIM. A_m will then used to derive the other required parameters and validate the theoretical model. The development of the FEM model in COMSOL requires four fundamental steps:

- Geometry description
- Mesh generation
- Material and Physics definition
- Solving and post-processing of results

In the following sections, the aforementioned steps towards the development of the FEM model will be described in detail.

4.1.1. Geometry Description

In COMSOL, the model of the LDFIM is built according to the geometry outlined in the machine's forward model where the dimensions are used to draw and construct the FEM model accordingly. In reality, the machine will be lengthy and it is practical to analyze one section of its complete structure. With the aid of some physics features available in COMSOL, a single pole pair section of the machine will be constructed for the finite element analysis.

Hence, the machine's data for the shore and pod coils available in tables 3.4 and 3.5 are used to build the model's geometry COMSOL for a single pole pair as shown in figure 4.1

4.1.2. Mesh Generation

COMSOL offers a variety of options for the mesh to be generated for the model in terms of how fine the sub-domains are desired to be and in what sequence they are to be defined. For the purposes of this project, the mesh is selected to be fine and physics-controlled in order to pay close attention to specific areas such as the air gap and teeth of the shore coil. The generated mesh for the LDFIM FEM model is shown in figure 4.2

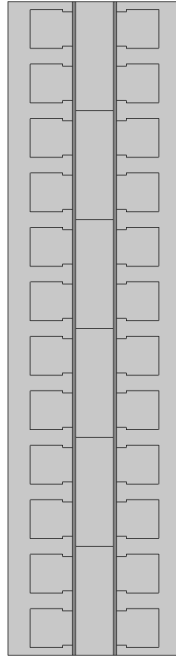


Figure 4.1: Geometry of LDFIM Pole Pair Model in COMSOL

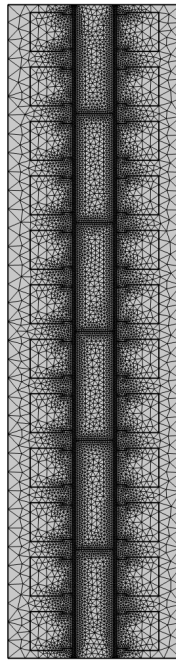


Figure 4.2: Generated Mesh of LDFIM Pole Pair Model in COMSOL

4.1.3. Material & Physics Definition

As previously mentioned, the purpose of the finite element analysis is to solve for the magnetic vector potential A_m . To achieve this, aspects related to the physics of the model are to be defined. In COMSOL, Ampere's law is defined for two components of the model notably, the air regions inside and outside the machine and the core regions of the shore coil. Prior to this, the materials required for the LDFIM model are defined. This

involves mainly the ferromagnetic material used to construct the shore's core which was selected previously and air for the rest of the model. Since a specific core material is to be used in this model, COMSOL offers the capability to define materials based on their properties. For this case, the core material is defined using its B-H curve from the manufacturer's datasheet which is shown in the figure 4.3.

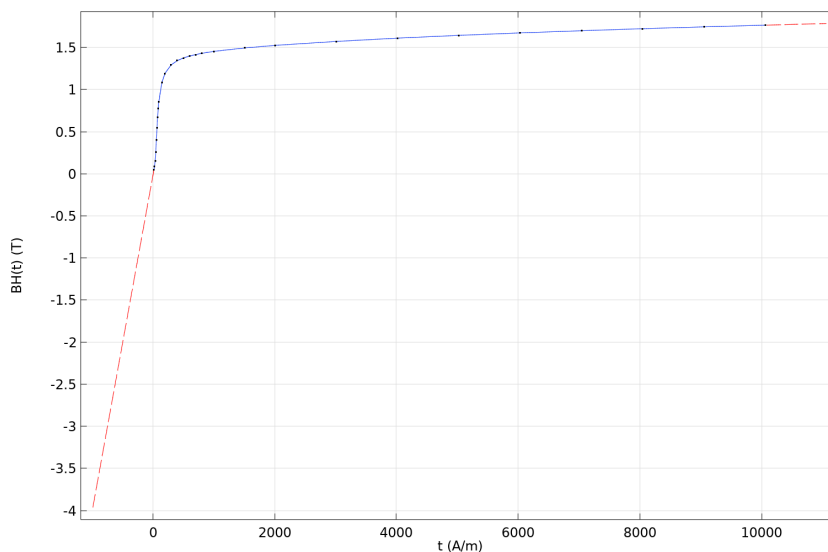


Figure 4.3: Core Material B-H Curve in COMSOL

As well as that, the LDFIM's model in COMSOL involved only one pole pair and this is possible with the periodic condition definition where the model is assumed to be linked at both ends. Moreover, the model needs to be magnetically insulated which is possible with the magnetic insulation physics definition. The remaining physics definitions are related to the coils of the pod and shore sides where the coil feature in COMSOL's magnetic fields problem is utilized.

4.1.4. Solving the FEM Model

After properly defining the materials of the model and the configuration of the coils according to the forward analytical model, the next task is to solve the model and obtain the relevant parameters to validate the theoretical results. This involves design of simulations to test the FEM model and obtain the results of interest. In the subsequent sections, the simulations applied to the model in COMSOL are discussed.

4.2. LDFIM FEM Simulations

In this phase of the project, the developed FEM model in COMSOL is tested in order to gather results. There are two main simulations to be applied in this case to validate the theoretical model. The first simulation is the no-load test where the following are validated:

- Air gap flux density
- Turns ratio
- Magnetizing and leakage inductances

The second simulation is the rated power test where the following are validated:

- Power transfer capability
- Efficiency

In the following sections, the simulations conducted on the model in COMSOL are discussed in detail.

4.2.1. LDFIM No-Load Test

In this simulation, the pod coil phases are kept open by setting their current to zero and the shore coil phases are energized with the value of the theoretically calculated magnetizing current at a specific phase. The magnetic behaviour of the model is then examined with particular focus on the air gap flux density which is plotted in figure 4.4.

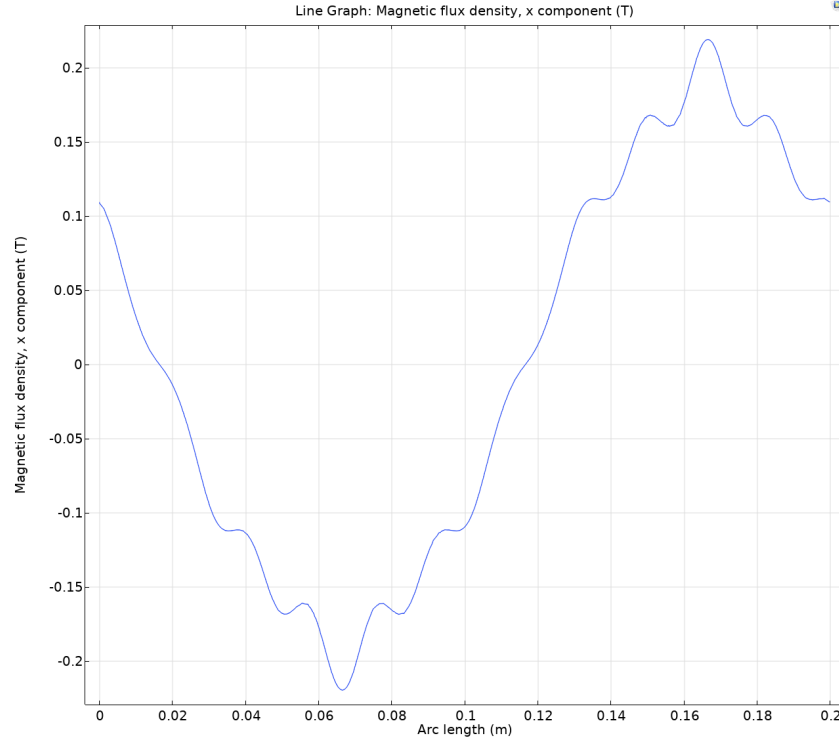


Figure 4.4: No-Load Air Gap Flux Density in COMSOL

The flux density in the plot is approximately sinusoidal with harmonic content due to the leakage inductances. In order to obtain the peak value of the fundamental flux density, the plot data is examined in MATLAB using Fourier analysis by applying the fast Fourier transform and the value obtained is $B_{g1} = 0.188T$ which is approximately the same as the analytically obtained value, the FEM model validates this aspect of the design.

The obtained value for the peak fundamental air gap flux density B_{g1} can then be used to calculate the main magnetizing inductance L_m from the COMSOL simulation data using the procedure outlined in [24] where:

$$L_m = \frac{\alpha_i B_{g1} \tau H k_{wshore} N_{shore}}{\sqrt{2} I_m} \quad (4.1)$$

The obtained value is $L_m = 773\mu H$ which is close to the theoretically calculated value. This then also validates the FEM model in this regard.

In order to obtain the primary side leakage inductances, the total inductance of the shore coil is obtained and the magnetizing inductance is subtracted from it. The main inductance of the shore coil is obtained by deriving the flux linkages on the primary side phases along with the coil currents and transforming the values into the alpha-beta reference frame in the following manner:

$$\begin{bmatrix} \Psi_\alpha \\ \Psi_\beta \\ \Psi_0 \end{bmatrix} = \frac{2}{3} \begin{bmatrix} 1 & -\frac{1}{2} & -\frac{1}{2} \\ 0 & \frac{\sqrt{3}}{2} & -\frac{\sqrt{3}}{2} \\ \frac{1}{2} & \frac{1}{2} & \frac{1}{2} \end{bmatrix} \begin{bmatrix} \Psi_a \\ \Psi_b \\ \Psi_c \end{bmatrix} \quad (4.2)$$

$$\begin{bmatrix} i_\alpha \\ i_\beta \\ i_0 \end{bmatrix} = \frac{2}{3} \begin{bmatrix} 1 & -\frac{1}{2} & -\frac{1}{2} \\ 0 & \frac{\sqrt{3}}{2} & -\frac{\sqrt{3}}{2} \\ \frac{1}{2} & \frac{1}{2} & \frac{1}{2} \end{bmatrix} \begin{bmatrix} i_a \\ i_b \\ i_c \end{bmatrix} \quad (4.3)$$

$$\begin{bmatrix} \Psi_\alpha \\ \Psi_\beta \\ \Psi_0 \end{bmatrix} = \begin{bmatrix} L_\alpha & & \\ & L_\beta & \\ & & L_0 \end{bmatrix} \begin{bmatrix} i_\alpha \\ i_\beta \\ i_0 \end{bmatrix} \quad (4.4)$$

Where L_α and L_β are the main inductances which are equal in magnitude since this is an induction machine[25]. The leakage inductance in the shore coil L_1 is then computed as:

$$L_1 = L_\alpha - L_m \quad (4.5)$$

The obtained leakage inductance is $L_1 = 102\mu H$ which is close to the sum of the slot and differential leakage inductances since COMSOL does not account for end-winding leakage due to the model being two-dimensional.

With regards to the leakage inductance in the secondary side, all sources of leakage other than the end connection were assumed to be insignificant in the analytical calculations. In order to verify this in the COMSOL simulation, the magnetizing current is applied to the pod coil windings while keeping the shore coil windings open. The air gap flux density and magnetizing inductance are calculated using the pod coil parameters in the same manner as for the primary side which is explained above. The calculated pod coil leakage inductance from the FEM simulation is $L_2 = 10nH$ which represents less than 1% of the calculated magnetizing inductance. Therefore, the theoretical assumption regarding the secondary side leakage inductance is validated.

In order to verify the theoretical value of the turns ratio k_{tr} , the no-load test is reversed and the currents are applied to the pod coil while keeping the shore coil phases open. The magnetizing inductance is calculated using the same procedure as before and the ratio of the two values of L_m from the COMSOL simulation will determine the turns ratio. The value obtained in the finite element analysis is 0.508 while the theoretically calculated value is 0.512. The small difference between the two values is due to the pod coil winding factor being overestimated since the winding function theory is used to calculate which can be inaccurate at times.

All of the results from the no-load test validate to a significant extent the theoretical model of the LDFIM in terms of magnetic properties and a summary is provided in the table below.

Parameter	Symbol	Analytical Value	Simulation Value	Unit
Air Gap Flux Density	B_{g1}	0.2	0.19	T
Magnetizing Inductance	L_m	819	773	μH
Primary Leakage Inductance	L_1	105	102	μH
Secondary Leakage Inductance	L_2	0	10	nH
Turns Ratio	k_{tr}	1.95	1.97	N/A

Table 4.1: No-Load Test Results

4.2.2. LDFIM Rated Power Test

Using the electrical circuit interface in COMSOL, the shore and pod coils are configured as part of a three phase electrical circuit model in which the shore coils are connected to current sources representing the input power and the pod coils are connected to resistors that model the battery load. The values of the devices in the circuit are set according to the forward analytical model data. Figure 4.5 demonstrates the electrical circuit that is developed in COMSOL for the purposes of the rated power test.

It is important to note that since the COMSOL model is a two-dimensional study, it will not account for the end-winding leakage inductances. Therefore, this is accounted for by adding inductors connected in series to each of the shore and pod coil windings according to the calculated values from the forward analytical model.

The rated power test is conducted in COMSOL by means of a frequency analysis where the LDFIM FEM model will be simulated at a specified AC frequency which is a critical parameter for the design and operation

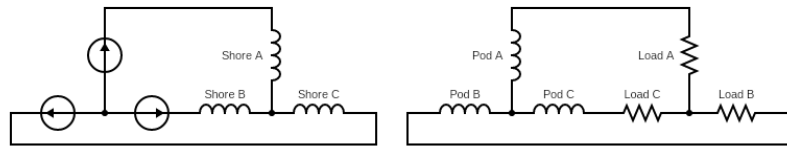


Figure 4.5: Electrical Circuit for Rated Power Test in COMSOL

of the machine as shown in the previous chapter. The frequency study for the rated power test is performed at $f = f_{shore}$. In order for the simulation to be conducted successfully, it is required to convert the B-H curve of the machine's core into an effective B-H curve that takes the hysteresis effect into account. Magnetic materials exhibit non-linear behavior and do not account for the full hysteresis loop when modeled in COMSOL. That is why it is required to generate a "cycle-averaged" B-H curve that would approximate the non-linear behavior of the material at the fundamental frequency. This is accomplished using a calculator as outlined in [26]. The effective B-H curve along with the original curve from the manufacturer's datasheet are shown in figure 4.6

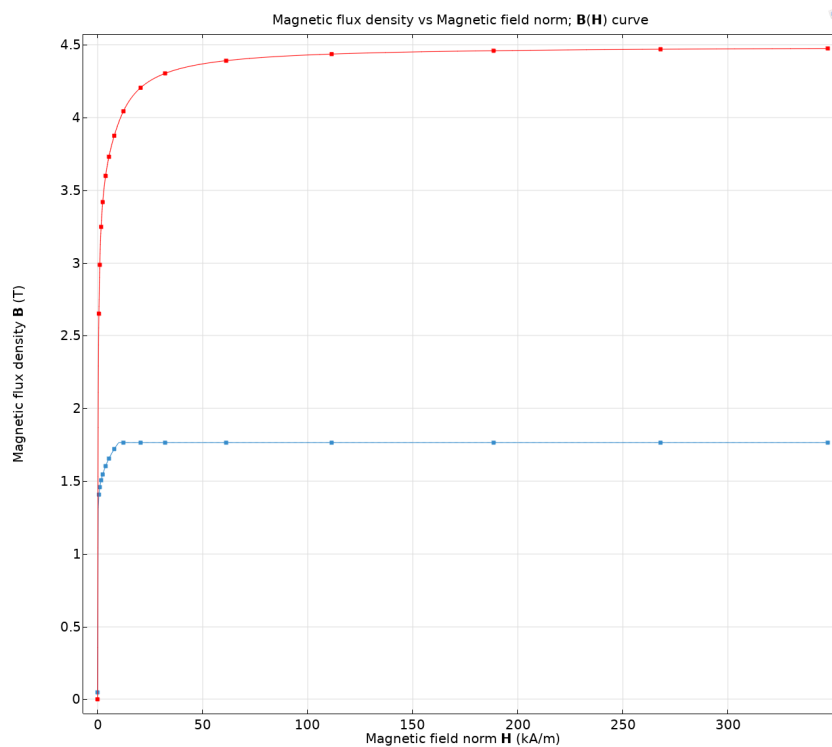


Figure 4.6: Plot of Standard B-H Curve (Blue) & Effective B-H Curve (Red)

After establishing the requirements for the rated power test, the model is simulated. In order to examine and analyze the magnetic behavior of the machine, the air gap flux density along with the magnetic flux density distribution in the model are plotted in figures 4.7 and 4.8 respectively.

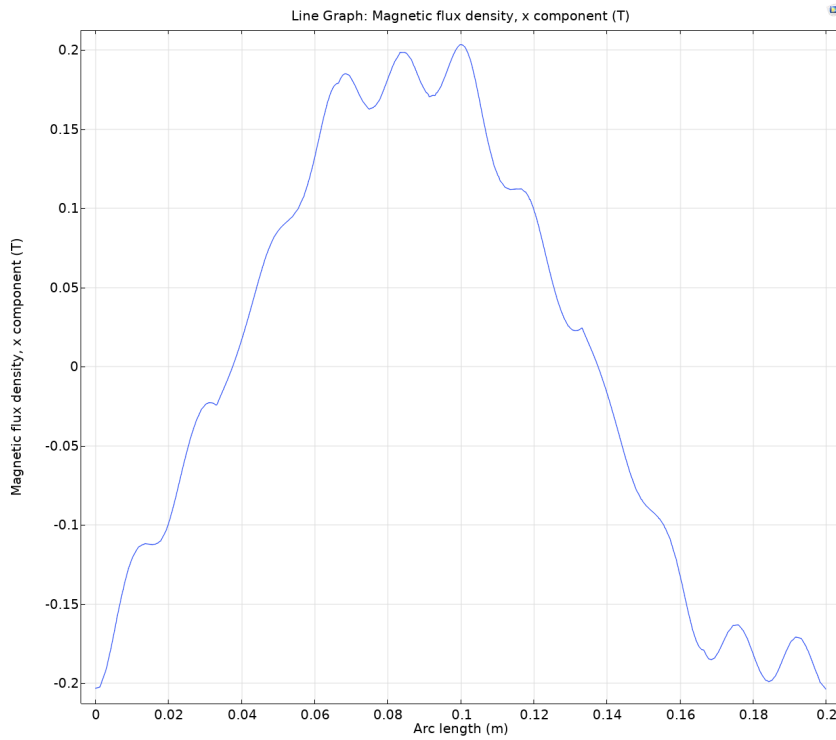


Figure 4.7: Plot of Air Gap Flux Density at Rated Power

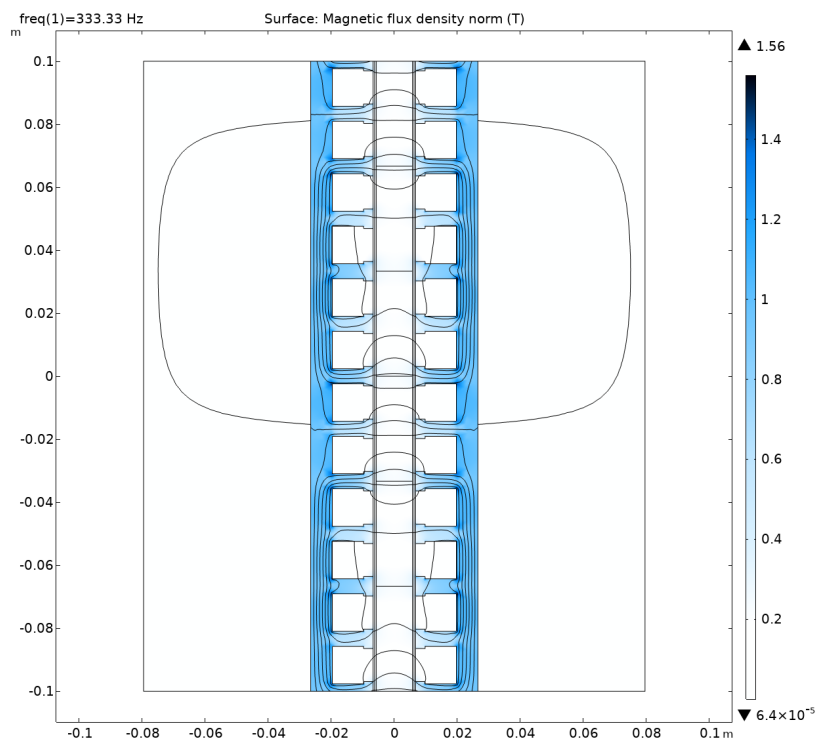


Figure 4.8: Plot of Magnetic Flux Density Norm in COMSOL

As shown in figure 4.7, the machine is properly magnetized since the peak value of the air gap flux density is approximately the same as the analytically calculated value and the result from the no-load test. Furthermore, figure 4.8 demonstrates that the flux distribution in the machine is spread effectively without saturating any section in the model above 1.6 T at full load.

In COMSOL, the input and output powers are computed using the derived calculations. Since the software is not able to calculate the core and winding losses directly, the losses in the rated power test will be calculated using the analytical method described in chapter 3 based on the FEM values. The required FEM results in order to calculate the losses from the simulation are the flux density in the core material, the peak value of the fundamental external magnetic field penetrating the pod coil and the currents flowing in the pod and shore coils. The primary side current will be exactly the same since it is fed directly as an input into the simulation model.

The FEM derived values required to analytically calculate the simulated losses are summarized in table 4.2 and are compared with the theoretical values.

Parameter	Symbol	Analytical Value	Simulation Value	Unit
Core Flux Density	B_c	1.6	1.57	T
Peak External Magnetic Field	\tilde{H}_{e1}	1.598e5	1.544e5	A/m
RMS Pod Coil Phase Current	I_{pod}	918	915	A

Table 4.2: COMSOL Loss Parameters

The calculated losses are then summed with the derived output power in order to accurately compute the input power and hence determine the simulated efficiency of the machine.

Table 4.3 summarizes the performance results of the rated power test.

Parameter	Symbol	Value	Unit
Parameter	Symbol	Value	Unit
Input Power	P_{in}	1.123	MW
Output Power	P_{out}	1.005	MW
Efficiency	η	89.53%	N/A

Table 4.3: LDFIM Simulation Performance Measures

As table 4.3 demonstrates, the machine is capable of transferring the rated power of 1 MW from the shore coils to the load resistors via the pod coils. The efficiency in the simulation is nearly equal to the theoretical result as the losses from both models are almost the same since the simulated magnetic properties are in agreement with the analytical values. Therefore, it is sufficient to rely on the COMSOL FEM simulations to determine that the machine was sized and designed properly in the analytical model since the theoretical results are in agreement with the simulation results.

5

LDFIM Multi-Objective Optimization

5.1. Background

In the previous chapters, an analytical model of the LDFIM is developed and validated theoretically using the equivalent circuit method and via simulation using the finite element method. It was shown that this specific machine can be designed to meet the requirements of the investigated vactrain system. The aim of the machine design so far was to prove the feasibility and compatibility of the machine in performing the wireless charging operation of the vactrain. In this chapter, the objective is to reach an optimum design where the performance of the LDFIM is enhanced as much as possible.

In machine design, the two most popular optimization algorithms are:

- Genetic Algorithm (GA)
- Particle Swarm Optimization (PSO)

There are several key differences between the two algorithms along with numerous advantages and disadvantages depending on their use in specific applications. No algorithm is necessarily better than the other as they take specific approaches to reach an optimal solution in an optimization problem. [27] provides a detailed overview of the several optimization techniques used and their benefits and limitations. With regards to the specifics of this thesis project, GA is more suitable given that it is able to produce a sufficiently accurate solution and it is available for direct computations using the MATLAB optimization toolbox without additional implementations from the user's side.

5.2. Development of GA Algorithm for LDFIM Optimization

There are several steps that need to be taken to implement the GA algorithm and develop a solution for the LDFIM optimization problem. GA is a search algorithm based on the principles of natural selection and natural genetics which involves the following fundamental operators:

- Selection
- Crossover
- Mutation

Subsequently, the following steps are required to perform the GA algorithm:

1. Random generation of initial population
2. Population evaluation and creation of an intermediate population by applying selection
3. Creation of the next population of potential solutions by applying crossover and mutation

An important aspect of the LDFIM optimization is the criteria applied to the design variables involved in the algorithm where the constraints of the parameters are defined in order to ensure that the final optimized design is geometrically feasible and a constraint on the output power will be applied to guarantee that the

generated designs will adhere to most important design objective and the results are pre-filtered prior to a final selection based on the performance of each design in the optimization objectives. Table 5.1 provides a summary of the optimization design variables and their constraints.

Design Variable	Symbol	Minimum	Maximum	Unit
Air Gap Flux Density	B_{ag}	0.1	0.5	T
Current Density	J	4e6	10e6	A/m^2
Ratio of Input Voltage to Induced Voltage	kV	1	2	N/A
Ratio of Slot Width to Slot Pitch	k_{slot}	0.2	0.725	N/A
Back Iron Height	h_y	6.5	15	mm
Pod Coil Conductor Area	A_{pod}	50	100	mm^2
Load Resistance	R_{load}	0.1	1	Ω
Efficiency & Power Factor Product	$\eta \cos \phi$	0.25	1	N/A

Table 5.1: Constraints on Optimization Design Variables

It is important to note that the design optimization of the LDFIM will mainly focus on the geometrical and electromagnetic aspects of the machine in order to enhance its performance. Design aspects such as the winding arrangement and configuration of the shore and pod coils have already been set previously in terms of the number of series connected turns and the coil distribution and pitch to achieve a suitable balance between the winding factor and the space harmonic content. The selected design parameters for the shore coil specifically in table 3.4 are intended to drastically reduce the fifth harmonic[21]. Moreover, certain assumptions regarding the design of the LDFIM are still valid in the optimization process such as the fill factor for conductors and the materials used for the core and coils.

The following remarks discuss the selection of the limits on the design variables:

- The air gap flux density B_{ag} is maintained at a relatively lower value due to the expected poor power factor of the machine and this will effectively also lower the required magnetizing current[16].
- The current density J is constrained to eliminate the use of active cooling if the value is too high and to reduce the conductor size if the value is too low[13].
- The input voltage is estimated from the induced voltage and their ratio k_V is confined to reduce the size and requirements of the power electronic converters supplying the shore coils.
- The ratio k_{slot} plays a crucial role in determining the structure of the shore coil and it must be kept within a certain range to prevent the design from having small teeth with high flux densities that could lead to saturation or from having excessive iron used with large teeth leading to higher core losses and less efficiency. This also applies to the back iron height h_y .
- The conductor area of the pod coil A_{pod} is restricted since using a large conductor area reduces the winding losses but increases the air gap length which reduces the power factor and vice versa.
- From the initial calculations, a suitable range is applied to the load resistance R_{load} to ensure that the machine can deliver the correct output power while optimizing the amount of current fed from the supply to limit the winding losses.
- The product $\eta \cos \phi$ is maintained within a practical range to estimate the primary side current and compute the shore coil geometry properly.

The optimization design variables summarized in table 5.1 are the starting point for the optimization design process by which the remaining properties of the LDFIM are defined and calculated. They effectively represent the search space of the algorithm which is limited in order to obtain designs of interest. Sufficiently narrowing the search space reduces the required time for computation and expedite the optimisation process without hindering it. Nevertheless, further constraints are required for the remaining parameters to maintain the geometric feasibility of the final design. Table 5.2 summarizes the constraints applied for the other design parameters.

The additional constraints summarized in table 5.2 are intended to ensure that the final design delivers the correct amount of output power and that the core material is not saturated beyond the maximum allowable flux density.

Design Parameter	Symbol	Minimum	Maximum	Unit
Output Power	P_{out}	0.99	1.01	MW
Flux Density in Shore Teeth	B_t	-	1.6	T
Flux Density in Shore Yoke	B_y	-	1.6	T

Table 5.2: Constraints on Optimization Design Parameters

The optimization problem of the LDFIM is multi-objective (MO) which results in a set of multiple solutions known as Pareto-optimal solutions. Pareto solutions satisfy the objectives of the optimization and no solution is more optimal than the other. Hence, the selection of the final solution to the problem is achieved by ranking the objectives and selecting the solution that fulfills the most weighted objectives. Therefore, the selected solution will compromise the other solutions that achieve the less weighted objectives[28].

In the LDFIM MO optimization, the objectives are defined and ranked in the following manner:

1. Minimize losses
2. Minimize the weight of the pod coil
3. Maximize the power factor

The objectives listed above are crucial to the performance and operation of the LDFIM. Reducing the losses, namely the copper and core losses, is the most important objective as it leads to an increase in the efficiency of the machine which would decrease the operating costs of the vactrain when charging at the stations. Similarly, the second most important objective is to lower the weight of the pod coil which is attached to the pod. This allows for light-weighting that is extremely beneficial for the launch of the vactrain. The last objective is to increase the power factor which would reduce the MVA requirements of the power converters at the station feeding the shore coil windings. It is important to note that improving the power factor will inevitably lead to an increase in the losses, impacting the efficiency of the machine negatively. This is the main conflict between the objectives and will play an important role in selecting the final solution from the Pareto set.

The GA algorithm for the MO optimization of the LDFIM is implemented in MATLAB by developing a fitness function describing the objectives of the optimization problem in addition to a constraints function enabling the Pareto solutions to conform to the design requirements and assumptions mentioned in chapter 3. These functions are described in-line with the analytical design methodology outlined in chapter 3 since the optimization algorithm is implemented on the analytical model that was verified and validated using the FEM as shown in chapter 4. Please note that objectives 1 and 2 are described explicitly in the fitness function while third objective is expressed as the complement of the power factor $1 - PF$, this is due to the fact that the GA algorithm will work on finding minimal design values for the optimization targets. Minimizing the complement of the power factor will increase its value.

5.3. Pareto Solutions & LDFIM Optimized Design

The implemented MO GA optimization generates a set of possible solutions, each having a set of design parameters that satisfy the specified constraints and enable the machine to operate according to the desired requirements with varying levels of performance in the defined objectives. Since it is difficult to evaluate the performance of each design for all three objectives, Pareto fronts for two objectives at a time will be analyzed in order to observe the optimization effect for each objective when compared to the other two objectives one at a time. This allows for a comprehensive study of the Pareto solutions before proceeding to the overall optimization involving all three objectives in order to come to the final optimal design of the LDFIM.

The Pareto front for objectives 1 and 2 along with the score histogram for both objectives are shown in figure 5.1. Figure 5.1 demonstrates the trend that with a heavier pod coil, the losses in the machine are reduced. Nevertheless, the range for the total loss is quite narrow since the two objectives in this case are not directly related given that there is also the weight of the shore coil to be considered which is not an optimization target. This Pareto front gives possible designs capable of limiting the losses to less than 75 kW with a pod coil mass in the range of 168-176 kg prompting significant improvements in the performance of the LDFIM for objectives 1 and 2 specifically.

The Pareto front for objectives 1 and 3 along with the score histogram for both objectives are shown in figure 5.2. Figure 5.2 shows the clear trend that a machine with a higher power factor will be less efficient as

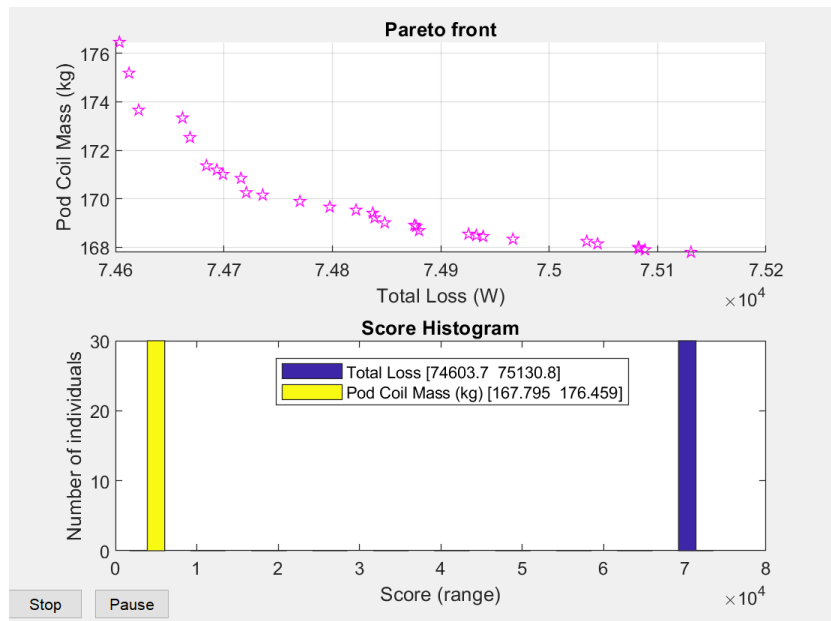


Figure 5.1: Generated Pareto Front & Score Histogram for Objectives 1 & 2

was hypothesised earlier. However, the optimization impact on the losses is far greater than its impact on the power factor which can be seen from the range of both objectives. The losses of the LDFIM can range from 75 kW to almost 120 kW while the power factor range is only from 0.38 to approximately 0.49. This clearly illustrates that there is a significant improvement in the efficiency while the power factor remains low below 0.5 for all possible designs. Hence, it is not beneficial to compromise the increased efficiency for a minor improvement in the power factor of the machine. This inference will be utilized in the overall optimized in order to come up with the final optimal design.

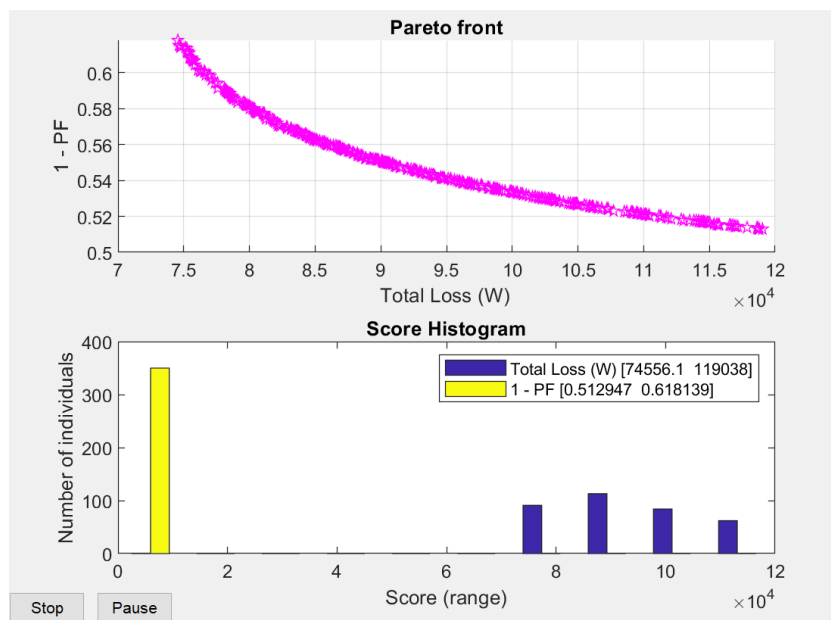


Figure 5.2: Generated Pareto Front & Score Histogram for Objectives 1 & 3

The Pareto front for objectives 2 and 3 along with the score histogram for both objectives are shown in figure 5.3. It can be observed that within a certain range, the power factor improves with a lighter pod coil. This inference agrees with the suggestion that the use of a lighter pod coil comes with a shorter coil width resulting in a smaller overall air gap length thus leading to an improved power factor. However, there are

other factors affecting the results that need to be taken into account such as the varying shore coil weight which is not an optimization target in this case as well. As with the optimization with objectives 1 and 3, the power factor is not improved beyond 0.5 for a reduced pod coil mass when compared with the initial design. Hence, it can be concluded at this point that the overall optimization will not contribute to a major improvement in the power factor of the machine and therefore, the efficiency and mass of the pod coil will be focused on primarily when selecting the final optimal design.

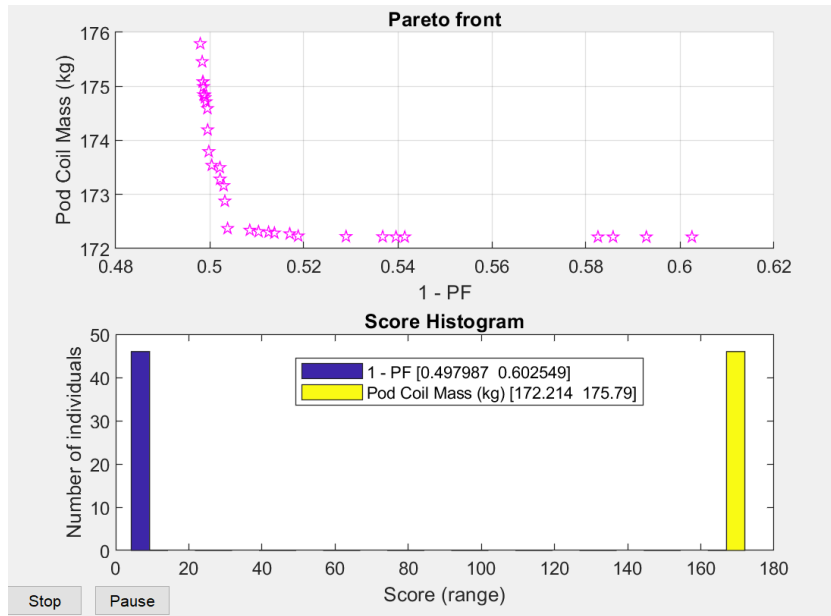


Figure 5.3: Generated Pareto Front & Score Histogram for Objectives 2 & 3

The Pareto front for objectives 1 and 2 along with the score histogram for all three objectives are shown in figure 5.4.

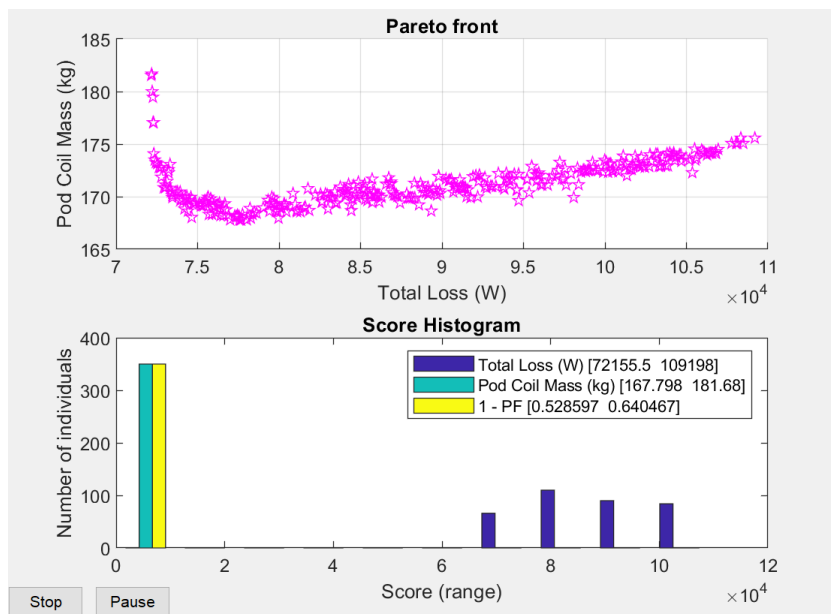


Figure 5.4: Generated Pareto Front & Score Histogram for LDFIM MO GA Optimization

The Pareto front in figure 5.4 has a dense plot with numerous possible solutions. This was achieved by adjusting the GA optimization options in MATLAB such as increasing the generations count and population size, and reducing the mutation rate. This enabled the search to be more refined and generated a sufficient

amount of solutions at the critical points. The task is to now select one final optimal solution. As shown in the score histogram, the range of the total losses in the Pareto front is much wider than that of the other objectives with the pod coil weight already being greatly improved when compared to the initial design. This essentially demonstrates that there are more significant improvements in the efficiency and pod coil weight of the machine in contrast to its power factor. This result facilitates the selection of the optimal design parameters for the LDFIM where the focus will be primarily on minimizing the losses as much as possible while having an acceptable value for the power factor. The final design parameters of the machine are tabulated below in comparison with the initial model. Please note that only the changed parameters are listed since the others are unchanged.

Parameter	Symbol	Initial Value	Optimized Value	Unit
Shore Coil Current Density	J_{shore}	10	5.78	A/mm^2
Shore Coil Conductor Area	A_{shore}	3.85e-5	5.455e-5	m^2
Shore Coil Slot Area	A_s	1.54e-4	2.182e-4	m^2
Shore Coil Slot Opening	w_s	0.0105	0.0104	m
Shore Coil Slot Height	h_s	0.0129	0.0201	m
Shore Coil Tooth width	w_t	0.0048	0.0058	m
Shore Coil Back Iron Height	h_y	0.0068	0.0085	m
Pod Coil Conductor Area	A_{pod}	9.25e-5	6.86e-5	m^2
Pod Coil Thickness	t	0.0115	0.0082	m
Magnetic Air Gap Length	g_e	0.0146	0.0113	m
Input Phase Voltage (RMS)	V_{in}	1130	1384	V
Shore Coil Resistance	R_1	0.0368	0.026	Ω
Pod Coil Resistance	R_{pod}	0.0639	0.0862	Ω
Load Resistance	R_{load}	1.5084	2.9213	Ω
Shore Coil Leakage Reactance	X_1	0.4941	0.6	Ω
Magnetizing Reactance	X_m	1.7157	2.21	Ω
Pod Coil Mass	pod_{mass}	228.5	169.5	kg
Air Gap Flux Density	B_{ag}	0.2	0.2633	T
Power Factor	PF	0.43	0.41	N/A
Input Power	P_{in}	1.12	1.077	MW
Efficiency	η	89.45%	92.75%	N/A

Table 5.3: Initial & Optimized Design Parameters

The results from table 5.3 show that there has been a significant improvement in the efficiency of the machine where it was increased by more than 3% and the weight of the pod coil was reduced by about 25%. These improvements were at the consequence of a slight decrease in the power factor of the machine and an increase in the dimensions of the shore coil's core and conductors. If an alternative solution with a slightly higher power factor was to be chosen, the efficiency would be less than in the initial case and this would be unacceptable. Since efficiency is the most important objective in this study, this solution for the optimization problem presents an excellent compromise between all three objectives.

It is important to note that the increase in the efficiency is mainly due to the reduction in the winding losses which was achieved by reducing the amount of current supplied to the coils and increasing the conductor area of the shore coil, effectively reducing its resistance and current density. Furthermore, the current density of the pod coil is maintained at the limit of $10 A/mm^2$ to keep a narrow coil width and thus maintain the power factor close to the initial value.

5.4. FEM Validation of LDFIM Optimized Design

Since the MO GA optimization algorithm was implemented on the analytical model, the optimization results deliver theoretical results that remain to be validated using FEM. Similarly to the previous chapter, a model was built in COMSOL based on the optimized design parameters and the same tests were applied in order to analyze the electromagnetic behavior of the optimized design for the machine and validate its performance.

5.4.1. Optimized LDFIM Geometry

The optimized design parameters are imported into COMSOL and the new model is built accordingly. Figure 5.5 shows the geometry of the optimized LDFIM.

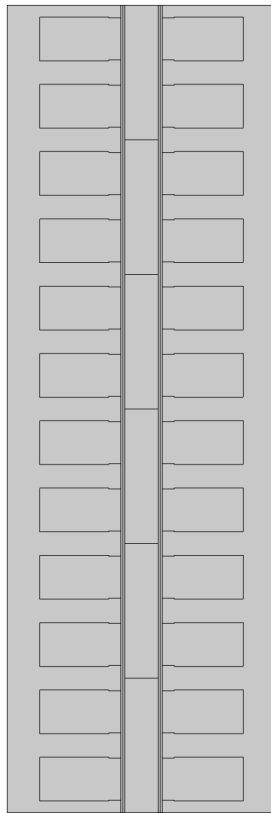


Figure 5.5: Optimized Geometry of LDFIM

From the optimized geometry of the machine in figure 5.5, it can be seen that the shore coil is augmented while the pod coil is reduced in size. The slots are now larger due to larger conductors and the width of the teeth along with the height of the back iron are also enlarged. Since the shore coil is attached to the track and is only built at the stations, an increase in the shore coil dimensions is allowable as it leads to a reduction in the size and weight of the pod coil in addition to an increase in the overall efficiency of the machine.

5.4.2. Optimized LDFIM No-Load Test

The no-load test is applied to the optimized model in the same manner as in the previous chapter. The air gap flux density is plotted in figure 5.6.

The no-load air gap flux density plotted in figure 5.6 has almost the same shape as the initial model but with more ringing due to a larger harmonic content. This is due to the enlarged slots causing more flux leakage than the initial design. Nevertheless, the peak value of the fundamental flux density is obtained using Fourier analysis and the calculated value is $B_{g1} = 0.245T$ which is close to the analytically computed value. Thus, this result validates the optimized design in this aspect.

Similarly to the previous chapter, the values of the magnetizing inductance, leakage inductances and the turns ratio are derived from the FEM model. The results are tabulated below in comparison to the analytical values.

All of the results from the no-load test validate to a significant extent the theoretical model of the LDFIM in terms of magnetic properties.

5.4.3. Optimized LDFIM Rated Power Test

As demonstrated in the previous chapter, the electrical circuit interface is used to build the same three phase system in order to apply the rated power and load to the machine while taking into account the end winding

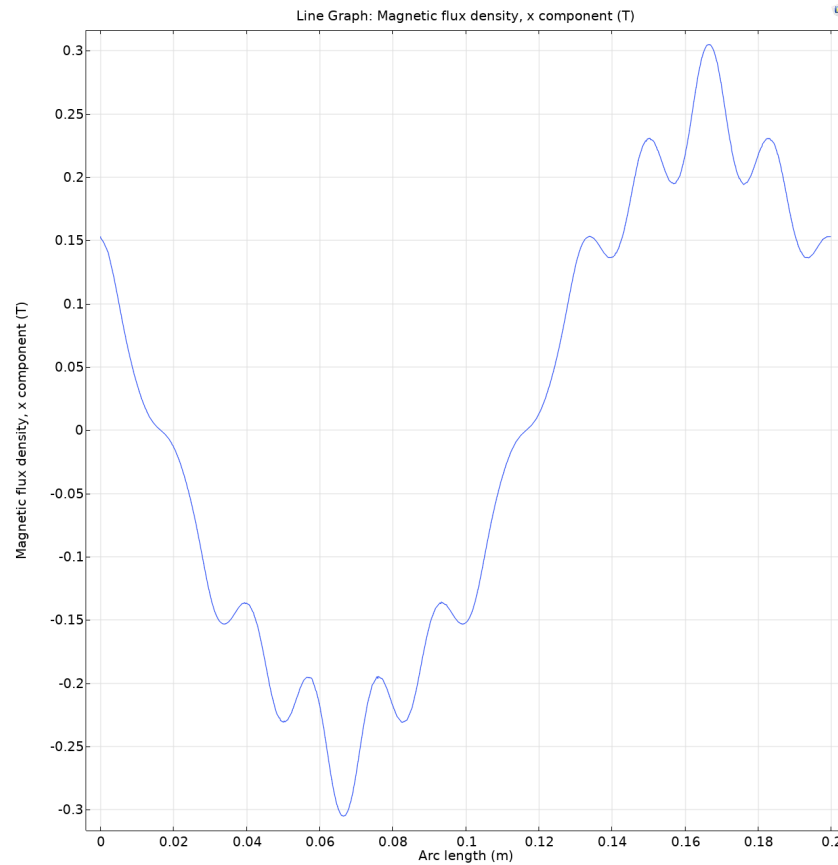


Figure 5.6: No-Load Air Gap Flux Density of Optimized LDFIM

Parameter	Symbol	Analytical Value	Simulation Value	Unit
Air Gap Flux Density	B_{g1}	0.2633	0.245	T
Magnetizing Inductance	L_m	1.1	1	mH
Primary Leakage Inductance	L_1	151	135	μ H
Secondary Leakage Inductance	L_2	0	8	nH
Turns Ratio	k_{tr}	1.95	1.97	N/A

Table 5.4: No-Load Test Results for Optimized LDFIM

leakage inductances on both sides. The rated power test is implemented in the same manner as before using a frequency analysis and using the effective B-H curve of the material.

The air gap flux density along with the magnetic flux density norm in the optimized model are plotted in figures 5.7 and 5.8 respectively.

As shown in figure 5.7, the machine is properly magnetized since the peak value of the air gap flux density is approximately the same as the analytically calculated value and the result from the no-load test. Furthermore, figure 5.8 demonstrates that the flux distribution in the machine is spread effectively with the maximum flux density in the core reaching around 1.6 T.

Using COMSOL, the output power of the optimized model is computed using the derived calculations and the input power is obtained by adding the losses which are calculated in the same manner as in chapter 4 using the analytical method described in chapter 3 based on the values extracted from FEM model of the optimized design table 5.5 summarizes the performance results of the rated power test.

Table 5.5 demonstrates that the optimized design of the machine is capable of transferring the rated power of 1 MW from the shore coils to the load resistors via the pod coils. There is an increase in the efficiency of the simulated optimized model in comparison to the initial simulated model where the effects of the optimization on the performance of the machine are clearly demonstrated.

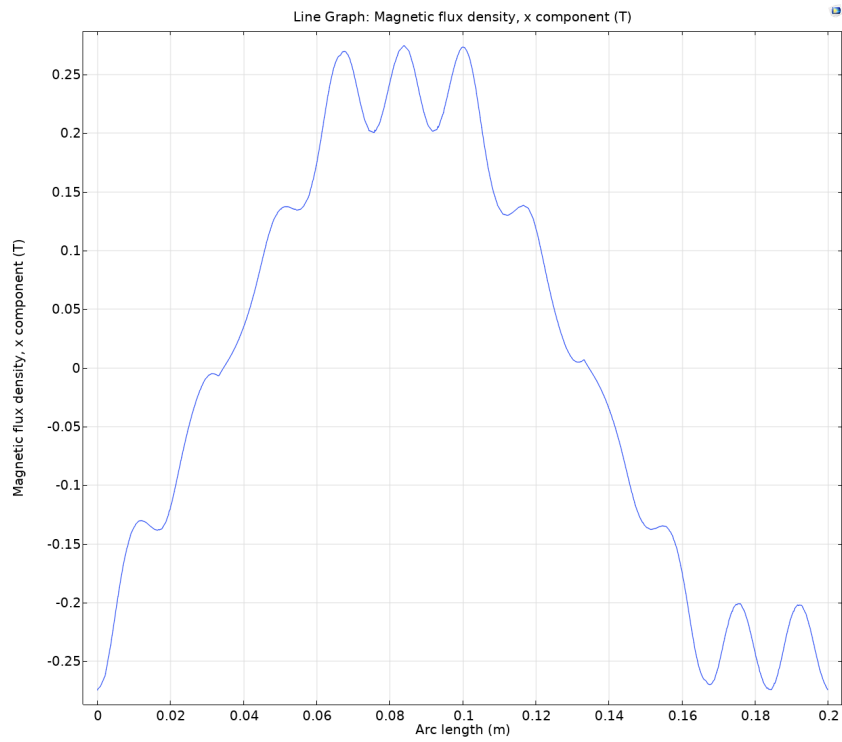


Figure 5.7: Plot of Air Gap Flux Density at Rated Power for Optimized LDFIM

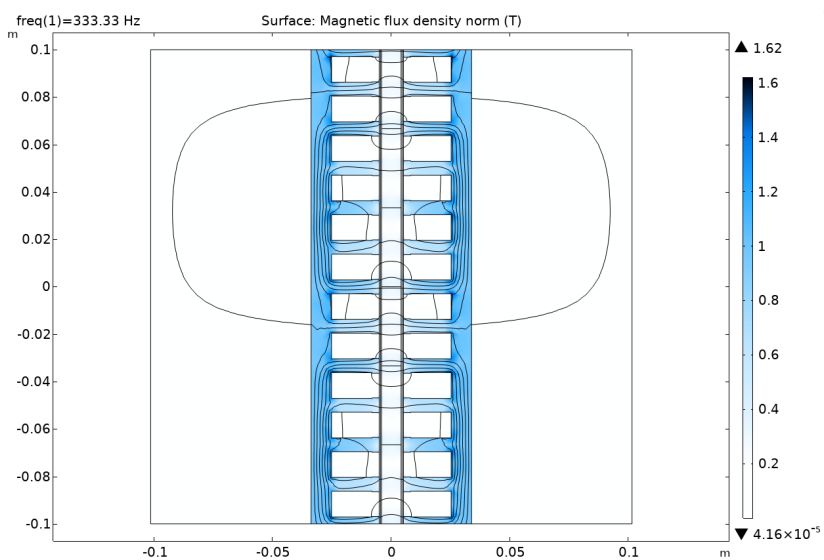


Figure 5.8: Plot of Magnetic Flux Density Norm for Optimized LDFIM

Parameter	Symbol	Value	Unit
Parameter	Symbol	Value	Unit
Input Power	P_{in}	1.07	MW
Output Power	P_{out}	0.99	MW
Efficiency	η	92.6%	N/A

Table 5.5: Optimized LDFIM Simulation Performance Measures

6

Investigated System Benchmarking Against Hyperloop

6.1. Investigated System Propulsion

The main focus of this thesis project so far in this report has been regarding the wireless charging operation using the LDFIM. The objective of this system is to integrate the charging mechanism into the propulsion system by incorporating a pod coil capable of interacting with different shore structures delivering various linear machines capable of serving multiple purposes such as charging, acceleration and cruising. It has already been established that the LDFIM is capable of performing the wireless charging operation. The aim in this part of the report is to provide an outlook on the propulsion of the vactrain and how the designed pod coil can achieve this function as well.

As mentioned in chapter 2, the preferred machine to accelerate the vactrain is the linear synchronous machine (LSM) as it is capable of delivering high thrust required to propel the vehicle to the desired cruising speed. For cruising, it is proposed to use a small rotating machine capable of speed-keeping since the drag is limited in the tube. As well as that, a wheel and axle system is to be used to provide suspension and movement on the tracks[1]. It is necessary to discuss the aforementioned aspects of the vactrain in order to have a complete view of the system before commencing the benchmarking study.

6.1.1. LSM for Vactrain Acceleration/Deceleration

The LSM is the suggested machine to accelerate and decelerate the vactrain. In this case, the pod coil becomes the primary side of the machine and it interacts with a secondary side fixed to the acceleration track. The purpose of the secondary side is to provide field excitation that interacts with the developed current density in the pod coil to produce thrust. The field excitation of the secondary side can be achieved using one of the following methods[8]:

- Permanent magnets (PM)
- DC excited coils (DCE)
- Superconducting magnets (SM)

The LSM using PM is shown in figure 6.1 as proposed in [1]. LSMs with PM or SM are usually built using an active guideway with the excitation element being on board the vehicle in a long primary configuration. Since this will be a short primary linear machine with the pod coil fixed to the vehicle, Using PM or SM is considered costly in terms of rare-earth material consumption for PM and the requirement of continuous active cooling using liquid nitrogen for SM considering that the acceleration track will be several kilometers long[8].

In this thesis, the suggestion is to use DCE LSM as it is considered to be a more feasible topology in terms of cost and material consumption. The machine in this configuration would be less efficient as compared to using PM or SM but with careful design, the losses can be mitigated and the machine can be developed to accelerate and decelerate the vactrain. Moreover, since the selected launch mode for this vactrain is constant

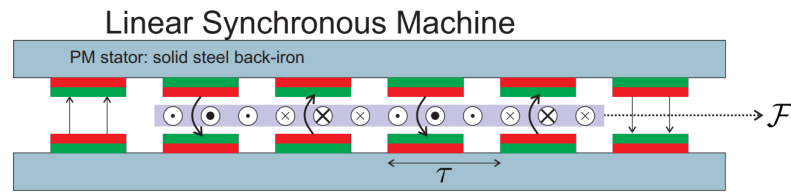


Figure 6.1: Top View of LSM Using PM[1]

acceleration followed by constant power whereby the rated power of the system is not exceeded, using DCE LSM allows for more freedom and flexibility in the control and operation of the machine. Initially, the flux produced by the excitation coils will be fixed at the highest starting value during constant acceleration. When the pod reaches the reference speed v_{ref} , constant power launch is applied in which the flux produced by the excitation coils is reduced as the speed of the vactrain is increased. This is achieved by maintaining the same current density in the pod coil during the complete acceleration stage and the voltage induced will also remain the same during the constant power phase where the frequency of the pod coil supply increases with increasing speed and flux of the secondary side decreases with decreasing thrust[1]. The flux produced by the excitation coils can be controlled by adjusting the amount of DC current fed into the windings and there is no need to activate all coils in the track but only the section where the pod is located at every instance in the acceleration/deceleration stage.

Additionally, the DCE LSM is similar to the LDFIM in terms of structure and configuration which is shown in figure 3.3 with the main difference being that the shore coil is the secondary side being fed with a DC supply. Essentially, using this type of LSM represents a continuation of the same track used to build the LDFIM and this can be used to establish the link between the two machines and evaluate the transition from the wireless charging operation to the acceleration of the pod. As mentioned in chapter 3, the LDFIM is used in the static charging operation where the vactrain is immobile at the station and it is important to analyze the shift from charging to propulsion. It was deduced in the design of the LDFIM that the machine cannot charge the on-board battery of the pod without producing thrust. Hence, it is required to place a mechanical break at the station to prevent any movement. Essentially, the pod would initially be accelerated with the thrust developed by the LDFIM after releasing the mechanical break and allow the pod to move. This thrust can be calculated by referring back to the fundamental sizing equation 3.19 and applying the results obtained from optimized performance of the machine. Table 6.1 provides a summary of the results related to the initial thrust of the vactrain using the LDFIM parameters:

Parameter	Symbol	Value	Unit
Peak Air Gap Flux Density	B_g	0.2633	T
Pod Coil Linear Current Density (RMS)	A	38.12	kA/m
Spatial Phase Shift between A & B Fundamentals	$\cos \zeta$	0.94	N/A
Thrust	F	15	kN

Table 6.1: LDFIM Thrust Parameters

Table 6.1 shows that the desired thrust is developed during the charging operation which will initially accelerate the pod out of the charging track with a starting acceleration of $a = 1.5m/s^2$ assuming a total pod mass of 10 tons. The DCE LSM will then resume the acceleration process in the manner described previously.

6.1.2. Vactrain Cruising Subsystem

The vactrain system is designed to be driven on wheels throughout the entire journey. Similar transportation systems claim that the traditional wheel and axle system cannot handle cruising speeds in the ultra-high range. As the desired cruising speed for the investigated system is set at $v_{max} = 700km/hr$, it is important to consider other examples where vehicles or modes of transport using wheels reached similar speeds. The current world record for the highest speed by a commercial train driving on steel wheels is set by the French TGV when it reached a speed of 574.8 km/hr in normal atmospheric pressure. As well as that, there are vehicles propelled by jet engines known as jet cars driving on pressed aluminium wheels which have set a land speed record of 1220 km/hr [1]. With such examples, it can be assumed that the vactrain can handle the intended

cruising speed using wheels to carry the pods.

6.2. Background on Hyperloop

After giving an overview of the investigated system, the objective is to benchmark it against a promising and well-known ultra-high speed transport system that is currently in development which is Hyperloop. The concept was initially developed by entrepreneur Elon Musk when he published a document titled "Hyperloop Alpha" in 2013 where he provided a blueprint for the development of Hyperloop and the economic and environmental incentives for investing in this system[29]. Ever since, there have been several firms and entities dedicated to further research into the concept and developing prototypes capable of delivering the performance standards outlined in [29]. Unfortunately, the Hyperloop designs currently in development remain confidential with minimal technical data being published. Hence, for the purposes of this study, the data for the Hyperloop system will be gathered from [29] where the technical data and details on the conceptual design of the system are presented, and also from [30] where detailed calculations are given to demonstrate the environmental impact of Hyperloop and other systems in terms of their energy consumption based on their intended design.

6.2.1. System Overview

Hyperloop as described in [29] is a system consisting of pods carrying passengers or freight traveling at ultra-high speed in low pressure tubes as shown in figure 6.2. The investigated system as shown in this report and in [1] is a similar concept in this regard. The main differences lie in the design and operation of the propulsion system which will be described and compared in the upcoming section.



Figure 6.2: Hyperloop Concept[31]

According to [29], Hyperloop will be launched using constant acceleration by means of a linear induction motor in long primary configuration where the required power for acceleration will be provided using an external power source. For cruising, the Hyperloop would consist of an air bearing system powered by an on-board propulsion system consisting of a compressor motor and battery. The system compresses the air building up in front of the pod while in motion and feeds it to the air bearing beneath the pod to provide suspension and motion. The power requirements in kW for the air bearing system to maintain the speed of the Hyperloop pod during cruising is given by the empirical formula 6.1 from [30]

$$P_{air} = 140 \times \frac{v}{c} + 247 \quad (6.1)$$

Where $\frac{v}{c}$ is ratio of the pod's speed to the speed of sound in air.

6.2.2. System Specifications

In this section of the report, the specifications of both systems are summarized prior to applying the two concepts in an application scenario in order to compare their performance. The general specifications of the two systems are summarized in table 6.2

Parameter	Investigated System	Hyperloop	Unit
Passenger Capacity	28	28	passenger/pod
Pod Payload	10000	15000	kg
Cruising Speed	700	1000	km/hr

Table 6.2: General Specification for Both Systems

The propulsion specifications of the two systems are summarized in table 6.3

Parameter	Investigated System	Hyperloop	Unit
Launch Mode	Constant Power	Constant Acceleration	N/A
Maximum Acceleration	1.5	4.9	m/s^2
Rated Power	1	21	MW
Acceleration Distance	21.65	7.88	km
Acceleration Time	3:30	0:57	min
Mass of Active Track Coil	68.7	800	kg/m
Cruising System	Wheels	Air Bearings	N/A
Cruising Power	100	364	kW

Table 6.3: Propulsion Specification for Both Systems

The information presented in tables 6.2 and 6.3 will be the input parameters to the benchmarking study for both systems. As shown in table 6.2, even though the two systems have the same passenger capacity, the Hyperloop pod features additional payload due to the incorporation of the air bearing system and its on-board propulsion system[29].

6.3. Suggested Application Scenario

6.3.1. Selected Journey

For this benchmarking study, the suggested scenario to which the two concepts will be applied is the journey between the cities of Dammam and Jeddah via the capital city Riyadh in the Kingdom of Saudi Arabia. This is a long distance journey of approximately 1275 km which takes almost 13 hours by driving and more than 2 hours by flight. The journey path is shown in figure 6.3.

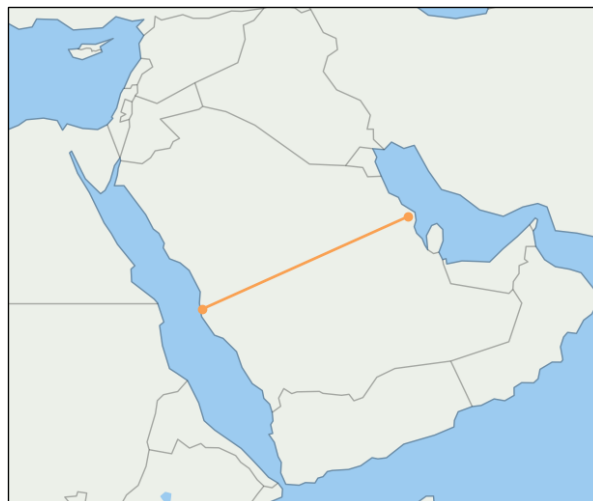


Figure 6.3: Suggested route for proposed vactrain system

The selected application scenario enables the use of the two systems to be of great value economically and environmentally. The systems fall in the category of ultra-high speed rail and thus they should be used in long distance travel where they can prove their potential and make a difference. Moreover, the nation of Saudi Arabia is already in talks with the company Virgin Hyperloop as reported in [32] to build a Hyperloop system for the country as shown in 6.4. The long term objective is to not only link major cities in the kingdom but the gulf region as a whole as shown in figure 6.5. It is aimed through this benchmarking study to show the intended impact of the Hyperloop concept and the potential of the investigated system in providing an ultra-high speed transportation service in this part of the world.



Figure 6.4: Hyperloop Pod for the Kingdom of Saudi Arabia[32]



Figure 6.5: Future plans for Hyperloop network in the Gulf region[33]

6.3.2. Investigated System Storage Specifications

For this specific application scenario, the on-board storage for the pod of the investigated system needs to be properly sized. As well as that, a suitable battery technology must be selected. Table 6.4 outlines the storage specifications of the investigated system

Parameter	Value	Unit
Battery Technology	Lithium Polymer (LiPo)	N/A
Specific Energy Density	200	Wh/kg
Ratio of Battery Mass to Pod Mass	12%	N/A

Table 6.4: Investigated System Storage Specifications

As mentioned in [1], the suggested battery technology for the on-board storage is Lithium Polymer (LiPo) which features one of the highest energy densities in the market. This helps in achieving a suitable battery mass capable of completing the required journeys in the application scenario.

6.3.3. Assumptions

The following assumptions are made regarding the application scenario:

- Initial state of charge of investigated system is 20%
- Charging at stations can occur while passengers are disembarking/embarking
- Most and if not all of the kinetic energy gained during launch is recovered during deceleration
- All non-propulsion loads are the same
- Both systems spend the same amount of time at stations between journeys

6.4. Results

The parameters of the systems are fed into a MATLAB script and calculations are made to estimate the performance of both concepts in the application scenario. In the following sections, the results are summarized.

6.4.1. Journey 1: Dammam to Riyadh

The results from the first journey are given in table 6.5 and the specific journey path is shown in figure 6.6

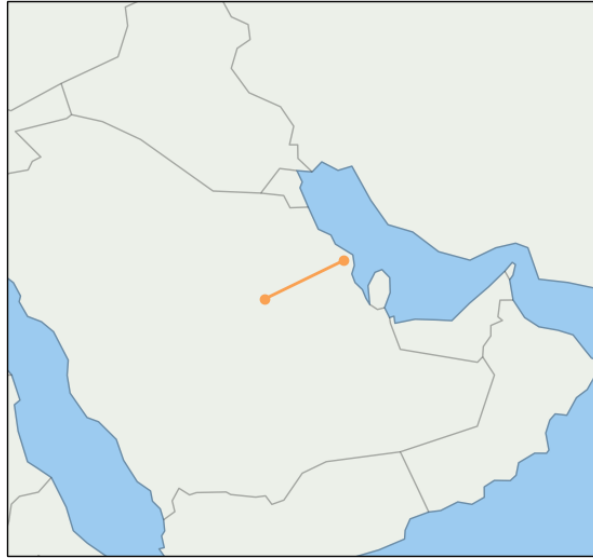


Figure 6.6: Journey 1 Path

Parameter	Value	Unit
Distance	400	km
Investigated System Charging Time	6	min
Investigated System Journey Time	38	min
Hyperloop Journey Time	25	min

Table 6.5: Journey 1 Results

6.4.2. Journey 2: Riyadh to Jeddah

The results from the second journey are given in table 6.6 and the specific journey path is shown in figure 6.7



Figure 6.7: Journey 2 Path

Parameter	Value	Unit
Distance	875	km
Investigated System Charging Time	7	min
Investigated System Journey Time	1:18	hr
Hyperloop Journey Time	53	min

Table 6.6: Journey 2 Results

6.4.3. Complete Journey: Dammam to Jeddah

The results from the full journey are given in table 6.7

Parameter	Value	Unit
Distance	1275	km
Investigated System Journey Time	2:03	hr
Hyperloop Journey Time	1:25	hr
Investigated System Energy Consumption	4.5	Wh/km/passenger
Hyperloop Energy Consumption	17	Wh/km/passenger

Table 6.7: Complete Journey Results

6.4.4. Investigated System Journey Profiles

The speed, thrust, specific energy and state of charge of the investigated system are plotted against the journey time are plotted in figure 6.8

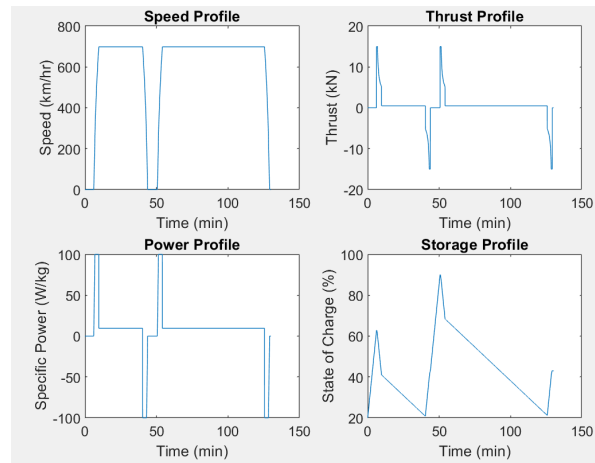


Figure 6.8: Investigated System Journey Profiles

As shown in figure 6.8, the specific power of the investigated system is maintained at 100 W/kg during acceleration and deceleration and this is in agreement with the desired launch mode. Moreover, this is also observed in the thrust profile of the vactrain which is constant during the constant acceleration phase and gradually reduces in the constant power phase until the pod reaches the cruising speed. Moreover, the state of charge of the on-board battery is always maintained above 20% and below 90% to maintain its lifetime and this is achieved by properly sizing the battery as a fraction of the total pod payload.

6.4.5. Performance Comparison

The speed and specific power profiles are plotted against the journey time for both systems in figure 6.9

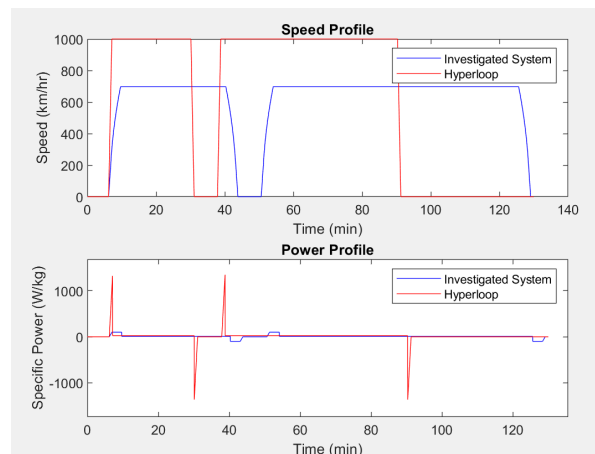


Figure 6.9: Speed & Specific Power Profiles for the Two Systems

Figure 6.9 shows that the Hyperloop pod reaches a higher cruising speed and thereby requiring less time to complete the entire journey. However, it requires a much higher peak power during the acceleration and deceleration phases reaching up to 21 MW as mentioned in [29] and since this must be provided by an external source, it would cause a significantly greater impact on the grid. This is the result of deploying a pod of greater mass and using constant acceleration for its launch. As well as that, the air bearing system required by the Hyperloop pod for suspension and cruising results in a higher energy consumption as compared to the investigated system.

6.5. Benchmarking

After obtaining the results from the application of the two concepts in the selected scenario, it is necessary to benchmark the investigated system against its counterpart. The following metrics are used in the benchmarking study to compare the two systems:

- Cruising Speed
- Power Demand
- Energy Consumption
- Material Usage
- Passenger Comfort

For each metric in the list above, the two systems are evaluated based on their specifications. The cruising speed and energy consumption have already been discussed. The power demand is inspected in order to estimate the system's impact on the grid if the latter is the supply and this can be evaluated based on the rated power of the systems. The material usage is assessed based on the mass of the material required to build the active track coils and the passenger comfort is estimated from the acceleration values. The two systems are compared and are given a normalised scores in the range from 1 to 10. The scores are then compiled to produce a radar plot which allows for a comprehensive and holistic assessment of both concepts for the different metrics. The radar plot is presented in figure 6.10

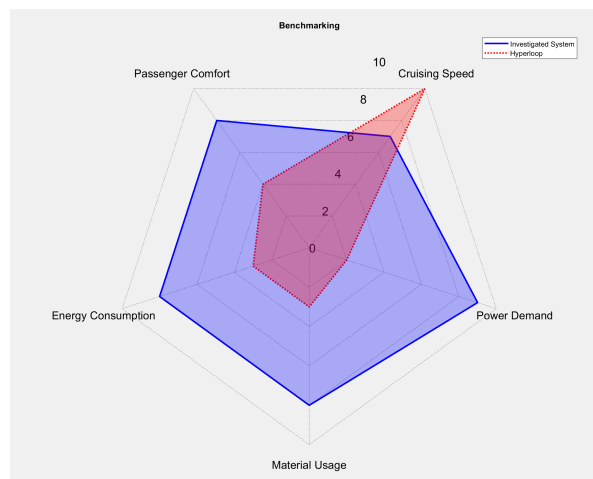


Figure 6.10: Benchmarking Radar Plot

The radar plot in figure 6.10 demonstrates that the Hyperloop system is only capable of overcoming the investigated system in terms of cruising speed. It definitely falls short in all of the other categories. By using a lower speed, the investigated system is able to attain much better performance in the other metrics. The main objective of this benchmarking study is to show the potential of the investigated system in competing with Hyperloop and not to conclude that any of the systems is essentially better than the other since their performance requirements are inherently different even though they serve the same function.

7

Conclusions & Recommendations

7.1. Conclusions

There is currently a transition towards all-electric mobility in the transportation sector. Novel systems such as Hyperloop and Maglev are intended to provide a sustainable alternative to air travel at least on the local scale. However, the aforementioned systems are considered to be lossy in terms of the sub-systems that are suggested to be used for their suspension and propulsion. In this project, a novel ultra-high speed rail system inspired by Hyperloop's concept of using evacuated tubes to provide a low pressure medium where pods carrying passengers can travel with minimal drag is investigated[1]. The aim is to reduce the energy requirements by using wheels for suspension and a linear motor for propulsion. Moreover, the investigated system aims to integrate the power supply with the propulsion mechanism by using an on-board battery supplying the vactrain during operation. At stations, the system's battery will be charged using a Linear Doubly Fed Induction Machine (LDFIM) and is then accelerated using a Linear Synchronous Machine (LSM). The main focus of this project was the design, optimization and validation of the LDFIM in performing the wireless charging operation of the system and the following conclusions were drawn over the course of this project:

- There were several challenges in achieving the project's objectives as induction machines are not commonly used for wireless power transfer and especially not their linear versions due to their poor power factor.
- Since the aim of this system is to incorporate a winding on-board the moving vehicle capable of interacting with different track structures to form various linear machines to operate the system, the most suitable machine to supply power is the LDFIM.
- It was demonstrated that this specific machine is capable of charging the system's battery with a sufficiently high efficiency and there was further improvement in its performance in the optimization process.
- The main problem which remains is the poor power factor which is inevitable due to the topology of the machine. Nevertheless, the problem is limited to the stations where the train's battery is being charged. Hence, there are possible solutions where special equipment capable of power factor correctness such as synchronous capacitors can be used locally at the stations to alleviate the problem[23].

After delivering the project's main objectives, an outlook on the propulsion aspect of the vactrain is discussed where suggestions are given regarding the propulsion sub-systems to be used after the charging operation. Then, once a complete overview on the investigated system was presented, a benchmarking study was conducted to show its potential in rivaling another novel and common ultra-high speed system which is the Hyperloop. It was concluded that the investigated system has potential to reduce the energy and material requirements of ultra-high speed travel when compared to Hyperloop as it is intended to operate at a lower cruising speed. Essentially, no system is better than the other, both concepts have different objectives and requirements. Moreover, Hyperloop is still in the development phase and the final designs can potentially be quite different than what was anticipated in [29].

7.2. Recommendations & Suggestions for Future Work

Design of electrical machines is an intricate process requiring several iterations before arriving at an optimal design solution. Effectively, there is no perfect design for any machine as different designs perform in varying levels in the various performance criteria. Hence, in this section of the report, recommendations and suggestions for future work are given in order to continue further research into this investigated system:

- The type of slots used in this thesis is open slots. It is recommended to look into semi-closed or closed slots in order to limit the slot leakage and possibly improve the power factor of the machine.
- It is also suggested to try out different slot/pole combinations for the shore coil and assess their impact on the performance of the machine.
- Different winding schemes should be included in the optimization process for both shore and pod coils in order to obtain more comprehensive Pareto fronts and make a wiser selection for the final optimal design.
- It is recommended to vary the GA optimization options in MATLAB to produce denser Pareto fronts and to apply the optimization process directly into the COMSOL FEM model and possibly try PSO instead of GA to diversify the results.

Overall, the novel vactrain system investigated in this project is promising and after thorough further research into its other required components, a blueprint document like the "Hyperloop Alpha" should be published outlining all of the technical and non-technical aspects of the system and providing a road map towards its development by indicating the costs of implementation and operation and also presenting details on the positive financial and environmental impacts the system can have in the future.

Bibliography

- [1] A. Veltman, P. V. D. Hulst, M. Jonker, and H. Polinder, "Tunnel-vision on economic linear propulsion?" *2019 12th International Symposium on Linear Drives for Industry Applications (LDIA)*, 2019. DOI: 10.1109/ldia.2019.8771014.
- [2] *Railway handbook 2017 – analysis*. [Online]. Available: <https://www.iea.org/reports/railway-handbook-2017>.
- [3] L. Wright, *Plane, train, or automobile? the climate impact of transport is surprisingly complicated*, Apr. 2020. [Online]. Available: <https://theconversation.com/plane-train-or-automobile-the-climate-impact-of-transport-is-surprisingly-complicated-117350>.
- [4] M. Flankl, T. Wellerdieck, A. Tüysüz, and J. W. Kolar, "Scaling laws for the electrodynamic suspension in high-speed transportation," *IET Electric Power Applications*, vol. 12, no. 3, pp. 357–364, 2017. DOI: 10.1049/iet-epa.2017.0480.
- [5] A. Weber, *Lightweighting is top priority for automotive industry*, Jun. 2018. [Online]. Available: <https://www.assemblymag.com/articles/94341-lightweighting-is-top-priority-for-automotive-industry>.
- [6] A. Filippone, "Mission analysis," in *Advanced Aircraft Flight Performance*, ser. Cambridge Aerospace Series. Cambridge University Press, 2012, pp. 423–469. DOI: 10.1017/CB09781139161893.018.
- [7] L. W. Taylor, *The laws of motion under constant power*, Jul. 1930. [Online]. Available: <https://kb.osu.edu/handle/1811/2458>.
- [8] I. Boldea, *Linear Electric Machines, Drives, and Maglevs Handbook*. CRC Pr I Llc, 2017.
- [9] A. Becetti, *Linear induction machine design for coasting operation of ultra high-speed vacetrain*, 2020.
- [10] M. Kane, *Tesla model 3's ipm-synrm electric motor explained*, Dec. 2020. [Online]. Available: <https://insideevs.com/news/461811/video-tesla-model-3-electric-motor-explained/>.
- [11] J. Fletcher and J. Yang, "Introduction to the doubly-fed induction generator for wind power applications," in *Paths to Sustainable Energy*, J. Nathwani and A. Ng, Eds., Rijeka: IntechOpen, 2010, ch. 14. DOI: 10.5772/12889. [Online]. Available: <https://doi.org/10.5772/12889>.
- [12] S. A. Nasar and I. Boldea, *Linear motion electric machines*. Wiley, 1976.
- [13] J. F. Gieras, *Linear Induction Drives*. Clarendon Press, 1994.
- [14] P. C. Sen, *Principles of electric machines and power electronics*. Wiley, 1989.
- [15] Yicheng Chen and P. Pillay, "An improved formula for lamination core loss calculations in machines operating with high frequency and high flux density excitation," in *Conference Record of the 2002 IEEE Industry Applications Conference. 37th IAS Annual Meeting (Cat. No.02CH37344)*, vol. 2, 2002, 759–766 vol.2. DOI: 10.1109/IAS.2002.1042645.
- [16] J. Pyrhonen, T. Jokinen, and V. Hrabovcova, *Design of Rotating Electrical Machines*. Wiley, 2013, ISBN: 9781118701652. [Online]. Available: <https://books.google.com.qa/books?id=4SUIAQAQBAJ>.
- [17] A. Mohammadpour, A. Gandhi, and L. Parsa, "Winding factor calculation for analysis of back emf waveform in air-core permanent magnet linear synchronous motors," *IET Electric Power Applications*, vol. 6, no. 5, p. 253, 2012. DOI: 10.1049/iet-epa.2011.0292.
- [18] J. Dong, *Lecture note 1: Windings, flux linkage and inductances*.
- [19] T. D. Cox, "Development of novel linear drive machines," Ph.D. dissertation, University of Bath, 2008.
- [20] *Cold-rolled non-oriented electrical steel*. [Online]. Available: <http://www.ibaosteel.com/ibaosteel/index>.
- [21] I. Boldea and S. Nasar, *The Induction Machine Handbook*, ser. Electric Power Engineering Series. CRC Press, 2010, ISBN: 9781420042658. [Online]. Available: <https://books.google.nl/books?id=iQ7OBQAQBAJ>.

- [22] J. Mühlethaler, "Modeling and multi-objective optimization of inductive power components," en, Ph.D. dissertation, ETH Zurich, Zurich, 2012. DOI: 10.3929/ethz-a-007328104.
- [23] S. Chapman, *Electric Machinery Fundamentals*, ser. McGraw-Hill International Editions. WCB/McGraw-Hill, 1999, ISBN: 9780071161459. [Online]. Available: <https://books.google.nl/books?id=Jv7CAQAACAAJ>.
- [24] J. Nerg, J. Pyrhonen, and J. Partanen, "Finite element modeling of the magnetizing inductance of an induction motor as a function of torque," *IEEE Transactions on Magnetics*, vol. 40, no. 4, pp. 2047–2049, 2004. DOI: 10.1109/TMAG.2004.830232.
- [25] A. Veltman, D. Pulle, and R. de Doncker, *Fundamentals of Electrical Drives*, ser. Power Systems. Springer Netherlands, 2007, ISBN: 9781402055041. [Online]. Available: <https://books.google.nl/books?id=J6opskVfXj4C>.
- [26] N. Paudel, *Model magnetic materials in the frequency domain with an app*, Jan. 2016. [Online]. Available: <https://www.comsol.com/blogs/model-magnetic-materials-in-the-frequency-domain-with-an-app/>.
- [27] Z. Abdmouleh, A. Gastli, L. Ben-Brahim, M. Haouari, and N. A. Al-Emadi, "Review of optimization techniques applied for the integration of distributed generation from renewable energy sources," *Renewable Energy*, vol. 113, pp. 266–280, 2017, ISSN: 0960-1481. DOI: <https://doi.org/10.1016/j.renene.2017.05.087>. [Online]. Available: <https://www.sciencedirect.com/science/article/pii/S0960148117304822>.
- [28] Y.-D. Chun, P.-W. Han, J.-H. Choi, and D.-H. Koo, "Multiobjective optimization of three-phase induction motor design based on genetic algorithm," in *2008 18th International Conference on Electrical Machines*, 2008, pp. 1–4. DOI: 10.1109/ICELMACH.2008.4800013.
- [29] E. Musk, *Hyperloop alpha*, 2013.
- [30] M. Janić, "Estimation of direct energy consumption and co2 emission by high speed rail, transrapid maglev and hyperloop passenger transport systems," *International Journal of Sustainable Transportation*, vol. 15, no. 9, pp. 696–717, 2021. DOI: 10.1080/15568318.2020.1789780. eprint: <https://doi.org/10.1080/15568318.2020.1789780>. [Online]. Available: <https://doi.org/10.1080/15568318.2020.1789780>.
- [31] M. H. Wong, *Hyperloop, the superfast 'vacuum train,' is coming to china*, Jul. 2018. [Online]. Available: <https://edition.cnn.com/travel/article/first-hyperloop-in-guizhou-china/index.html>.
- [32] A. Buller, *Virgin hyperloop eyes commercial pilot by 2024, says ceo*, Apr. 2021. [Online]. Available: <https://www.arabianbusiness.com/transport/462491-saudi-arabia-could-see-virgin-hyperloop-commercial-pilot-by-2024-says-ceo>.
- [33] *Hyperloop one can help transform the kingdom and be part of vision 2030 delivery*. [Online]. Available: <https://www.materialbidders.com/mb-news-details.php?id=53>.